Towards routine shipborne measurements of columnar CO$_2$, CH$_4$, CO, and NO$_2$: a case study for tracking regional-scale emission patterns

Vincent Enders[1,2], Astrid Müller[3], Matthias Max Frey[3,4], Frank Hase[4], Ralph Kleinschek[1], Marvin Knapp[1,5], Benedikt Löw[1], Isamu Morino[3], Shin-Ichiro Nakaoka[3], Hideki Nara[3], Hiroshi Tanimoto[3], Sanam N. Vardag[1,6], Karolin Voss[1], and André Butz[1,6]

[1]Institute of Environmental Physics (IUP), Heidelberg University, Heidelberg, Germany
[2]Institute of Materials Chemistry, TU Wien, Vienna, Austria
[3]National Institute for Environmental Studies (NIES), Tsukuba, Japan
[4]Institute of Meteorology and Climate Research (IMKASF), Karlsruhe Institute of Technology (KIT), Karlsruhe, Germany
[5]Harvard John A. Paulson School of Engineering and Applied Sciences, Harvard University, Cambridge, MA, USA
[6]Heidelberg Center for the Environment (HCE), Heidelberg University, Heidelberg, Germany

Correspondence: André Butz (andre.butz@uni-heidelberg.de), Hiroshi Tanimoto (tanimoto@nies.go.jp)

Abstract. Mobile remote sensing observations from shipborne platforms offer a unique opportunity for validating satellite observations and sampling plumes of greenhouse gases and short-lived air pollutants from the world's highly populated coastal megacities and industrial sites. Here, we demonstrate the capabilities of a shipborne setup that combines a sun-viewing EM27/SUN Fourier transform spectrometer for the shortwave-infrared spectral range with a DOAS (Differential Optical Ab-

5   sorption Spectroscopy) spectrometer for the visible spectral range, enabling simultaneous measurements of the column abundances of carbon dioxide (CO$_2$), methane (CH$_4$), carbon monoxide (CO), and nitrogen dioxide (NO$_2$). For several months in 2023 and 2024, the instruments were operating autonomously on a commercial vessel traveling back and forth along the coast of Japan. We show that, for CO$_2$, CH$_4$, and CO, precision and repeatability comply with the standards of the Collaborative Carbon Column Observing Network (COCCON). Further, for a case study in the vicinity of Nagoya, we demonstrate the

10   scientific leverage of this mobile multi-species approach: Simultaneous measurement of CO$_2$, CO, and NO$_2$ enhancements is used to successfully disentangle emissions from different sources. Our study demonstrates that routine shipborne deployment is possible. The setup delivers highly precise and accurate concentration records of the target species, as required for satellite validation, and enables emission monitoring of sources due to their distinct emission ratios.

Graphical abstract
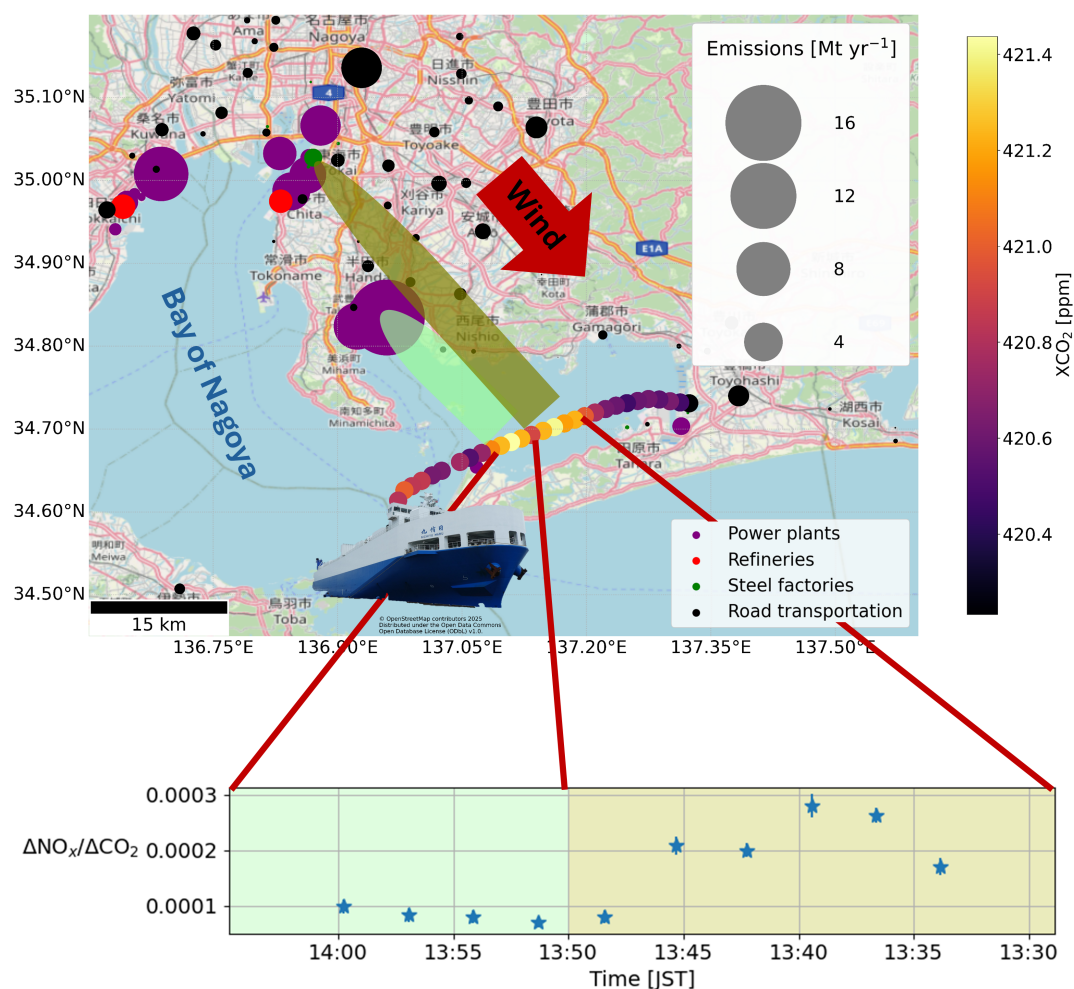
1 Introduction

The greenhouse gases carbon dioxide (CO_2) and methane (CH_4) drive climate change and thus are subject to manifold activities that aim at monitoring and verifying their emission rates, as required for the Paris Climate Agreement. Measuring CO_2 and CH_4 atmospheric concentrations allows for independent verification of bottom-up statistical data and accounting reports

20 when inverse transport modeling is used to derive top-down emission estimates from the observed concentration gradients (e.g. Reuter et al. (2014), Wong et al. (2015), Jones et al. (2021)). In addition, concentration measurements of carbon monoxide (CO) and nitrogen dioxide (NO_2) can help attribute source type contributions for CO_2 since these air pollutants originate from combustion (together with CO_2) and the emission ratios between these three trace gases are specific to the processes and their

efficiencies involved (Guevara et al., 2024). CO and NO_2, themselves, have adverse effects on human health, and thus, moni-

25 toring is warranted (Chen et al., 2007; Manisalidis et al., 2020).

Most commonly, atmospheric concentrations of CO_2, CH_4, CO, and NO_2 can be measured through absorption spectroscopic techniques realized by in situ or remote sensing instruments. The latter have been deployed on satellites (e.g. Butz et al. (2011), Eldering et al. (2017), Van Geffen et al. (2022)), on airborne platforms (e.g. O'Shea et al. (2014), Krautwurst et al. (2017), Leifer et al. (2018)), or in ground-based networks (e.g. Dietrich et al. (2021), Luther et al. (2022), Herkommer et al. (2024)).

30 The Total Carbon Column Observing Network (TCCON; Wunch et al. (2011)) and the COllaborative Carbon Column Observing Network (COCCON; Frey et al. (2019)) host dozens of sun-viewing Fourier Transform Spectrometers (FTS) operating in the shortwave-infrared spectral range and providing the column-average dry-air mole fractions of CO_2 (XCO_2), CH_4 (XCH_4), and CO (XCO). The Pandonia Global Network (PGN) (Herman et al., 2009) provides NO_2 columns among other air pollutants. Primarily, these networks have been designed for validating observations by satellites such as GOSAT (CO_2, CH_4; Butz et al.

35 (2011)), OCO-2 (CO_2; Eldering et al. (2017)), GOSAT-2 (CO_2, CH_4, CO; Imasu et al. (2023)), OCO-3 (CO_2; Taylor et al. (2020)), Sentinel-5 Precursor (CH_4, CO, NO_2; Landgraf et al. (2016); Van Geffen et al. (2022)), GOSAT-GW (CO_2, CH_4, NO_2; Tanimoto et al. (2025)), and future missions such as CO_2M (CO_2, CH_4, NO_2; Sierk et al. (2021)), and TANGO (CO_2, CH_4, NO_2; Brenny et al. (2023); Charuvil Asokan et al. (2025)). Some of these missions use NO_2 not just as an informant for emission patterns but also, more technically, to geographically contour emission plumes from localized emitters such as

40 coal-fired power plants and urban centers, thereby assisting in CO_2 emission estimates (Kuhlmann et al., 2021; Yang et al., 2023). In addition to providing essential validation for these satellite data, the ground-based measurements such as conducted within the TCCON and COCCON also give valuable constraints on local to regional emission patterns (Wunch et al., 2009; Babenhauserheide et al., 2020; Frey et al., 2021; Kiel et al., 2021; Ohyama et al., 2023). Thereby, simultaneously measuring several substances provides the opportunity to selectively attribute concentration variability to specific sources by examining

45 concentration and emission ratios.

Butz et al. (2022) reviewed the challenges and opportunities of implementing a mobile variant of the COCCON spectrometer (EM27/SUN Fourier transform spectrometer, Bruker Optics, Germany). Ship deployments of such spectrometers are appealing since they provide satellite validation over the oceans, which are currently only sparsely covered with validation data (Müller et al., 2021). If the ships commute along coastlines, shipborne observations can potentially constrain emission outflow from

50 the upwind source regions. Here, we report on further development of our mobile COCCON spectrometer, whose ship deployment was showcased previously in Klappenbach et al. (2015), Knapp et al. (2021), and Butz et al. (2022), and which was used for land-based deployments to constrain localized emission patterns (Butz et al., 2017; Luther et al., 2019, 2022). This study introduces two key advances. First, we have successfully installed and remotely operated the mobile COCCON spectrometer on a commercial freighter that regularly sails Japan's coastline. Second, we co-mounted a DOAS unit measuring in the visible

55 spectral range that allows for retrieving total column NO_2 alongside XCO_2, XCH_4, and XCO delivered by the EM27/SUN instrument. Thereby, simultaneously measuring several substances provides the opportunity to selectively attribute concentration variability to specific sources by examining concentration and emission ratios. A case study on Nagoya Bay demonstrates the system's performance and shows how the combined trace-gas measurements enable source-selective emission verification.

2 Instrument setup

60 The instrument described in this work is an upgrade of a commercially available Bruker EM27/SUN Fourier-transform spectrometer (FTS) for the shortwave-infrared spectral range, recording the absorption features of CO_2, CH_4, CO, and O_2 (the latter for calculating mixing ratios) and a commercially available Ocean Optics QE-Pro spectrometer for the visible spectral range, resolving the individual absorption lines of NO_2, and potentially other trace gases in the future.

2.1 EM27/SUN FTS and solar tracker

65 The EM27/SUN FTS (Bruker Optics, Germany) is the standard instrument of the COCCON network for land-based observations of XCO_2, XCH_4, and XCO (Frey et al., 2019). Modifications and performance demonstrations for ship-based deployments are described in Klappenbach et al. (2015), Knapp et al. (2021), and Butz et al. (2022). Summarizing the most important features here, the EM27/SUN has an optical resolution of 0.5 cm^{-1} and a semi-field-of-view of 2.36 mrad (Gisi et al., 2012; Frey et al., 2015). The latest EM27/SUN version contains two detectors. The first InGaAs photodetector covers the spectral range

70 between 5500 and 11000 cm^{-1} (Gisi et al., 2012), where O_2, CO_2, and CH_4 absorption lines are present. The second InGaAs-detector with spectral extension towards the infrared covers the wavelength range between 4000 and 5500 cm^{-1} (Hase et al., 2016), where CO absorption features can be found. The EM27/SUN FTS demonstrated its versatility and robustness under various climatic conditions and in different settings (Butz et al., 2017; Viatte et al., 2017; Luther et al., 2019; Humpage et al., 2021; Frey et al., 2021), making it an ideal instrument for campaign deployments. In addition, Frey et al. (2019) demonstrated

75 its suitability in terms of stability and comparability for network applications such as those implemented through COCCON. Our EM27/SUN is operated and characterized according to COCCON protocols, with two modifications. First, to avoid data loss in the case of tracker instability, we record individual interferograms for each forward-backward scan rather than relying on automatic co-adding of 10. Second, we use an interferogram sampling rate of 20 kHz (instead of 10 kHz). This leads to one forward-backward scan being completed approximately every 15 seconds. In addition to this, the solar tracker of the standard

80 EM27/SUN is replaced by a custom-built system to be able to compensate for the rather quickly changing attitude and orientation of a ship platform. The high precision of our custom-built tracking system was demonstrated for shipborne deployments in Butz et al. (2022), and for balloonborne deployments in Voss et al. (2024), where more details on the tracking system can also be found. The instrument is housed in an aluminum box to protect it from harsh weather. The entire box is ventilated and equipped with various ancillary sensors for pressure and temperature measurements, and its position is tracked via GPS. Figure

85 1 shows the box with the instruments on board the commercial vessel *Nichiyu Maru* (Ocean Link, Ltd.) during the deployment described in Sect. 3.

2.2 DOAS spectrometer

To supplement the setup with measurement capabilities for NO_2, we co-mounted a grating spectrometer measuring solar absorption spectra in the visible (VIS) spectral range. Using differential optical absorption spectroscopy (DOAS) (Platt and

90 Stutz, 2008), NO_2 atmospheric column abundances are accessible. The DOAS instrument uses part of the light beam from the

Figure 1. Box housing the EM27/SUN FTS, the DOAS spectrometer, and the sun tracker assembly. The box is positioned on the upper deck of the vehicle-carrier *Nichiyu Maru* (Ocean Link, Ltd.).

solar tracker, which is not needed for the FTS. The solar beam is coupled into an optical fiber (Laser Components FVP-400) using a custom-built telescope assembly similar to the one used in Butz et al. (2017) and Voss et al. (2024). The assembly consists of the following components, as schematically shown in Fig. 2: A prism (Thorlabs PS910) positioned under total-reflection relays the incoming beam into a lens tube with a bandpass filter centered at 460 nm (Edmund Optics Hoya B460). The field of view of the telescope is limited to $1.15°$ by focusing the light onto an 800 μm aperture (Edmund Optics 34-445) using a bi-convex lens (Thorlabs LB1027-A). Furthermore, the light is diffused before entering the fiber by a polytetrafluorethylene reflector plate mounted at a $45°$ angle with respect to the optical axis. The fiber is mounted so that only light from the reflector plate can enter it. The fiber is connected to an Ocean Optics QE-Pro spectrometer operating in a Czerny-Turner configuration (Czerny and Turner, 1930) in the visible spectral range.

The technical data of the VIS spectrometer and the settings used during the deployment described in this work are listed in Table 1. The spectrometer entrance slit with a width of 100 μm defines the light throughput and the width of the spectral response function (SRF). The spectral sampling amounts to 5 detector pixels per full-width-at-half-maximum (FWHM) of the SRF, corresponding to 0.7 nm, as determined by measuring individual spectral emission lines from mercury and krypton emission lamps. The DOAS spectrometer is configured such that it records spectra in a wavelength range between 400.7 and 495.9 nm. Two different exposure times are used to maximize the signal but prevent saturation of the detector. At high solar zenith angles (SZA) during the morning and evening, spectra are recorded with an exposure time of 700 ms. At low SZA, the instrument is switched automatically to an exposure time of 350 ms.

A two-stage cooling is used to keep the DOAS spectrometer and its detector at constant temperatures. The first stage is the QE-Pro spectrometer's internal thermoelectric cooler (TEC). It can cool the detector down to 20 K below the ambient temperature. In addition, the spectrometer is housed inside a custom-built enclosure, which is sealed so that water vapor is prevented from
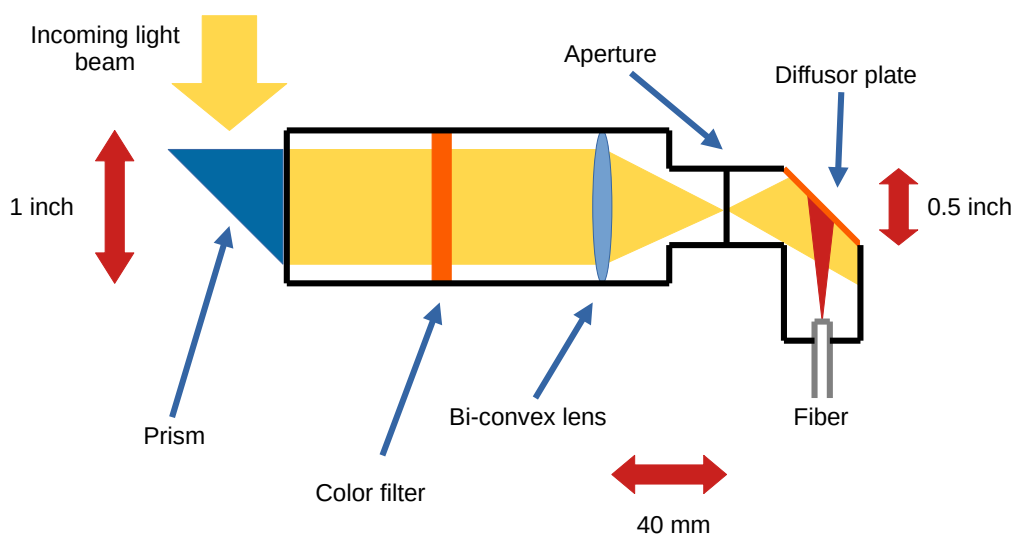
Figure 2. Schematics of the telescope of the DOAS instrument. The figure shows the telescope's components, including the prism, color filter, bi-convex lens, and aperture. The acceptance cone of the fiber, which is shown in red, indicates which part of the light beam is directed into the fiber. Drawing not to scale.

Detector	Hamamatsu S7031-1006
Number of pixels	1024
Pixel size area	24 μm^2
Resolution	0.7 nm
Peak quantum efficiency	90%
Integration time	350 and 700 ms
f-number	f/4
Entrance slit	100 μm x 1 mm
Internal TEC	27 °C
Wavelength range	400.7 - 495.9 nm

Table 1. Overview of the spectrometer specifications and the operational settings of the DOAS instrument during the deployment. Data partly taken from Ocean Optics, Inc. (2014).

entering by allowing exchange with the ambient air only through a silica gel tube. A second TEC is used to regulate the temperature inside this enclosure to an accuracy of ±0.1 K. This is, however, only possible for a temperature range of 2 K below and 15 K above the outside temperature. Since outside temperatures in the range between 0 °C and 40 °C occurred during the deployment, the external TEC was operated at temperatures between 10 °C and 38 °C, and the internal TEC at

115 temperatures of up to 27 °C, which is not ideal in terms of noise reduction but ensures temperature stability throughout the deployment. An upgrade of the external TEC facilitating stabilization at lower temperatures is planned for the future.

For the campaign reported here, the SRF of the DOAS spectrometer was recorded by measuring the emission lines of krypton or mercury lamps. We conducted these lamp measurements before and after the campaign deployment and approximately every six weeks while the instrument was onboard the ship. All SRFs show shape deviations of less than 4% relative to the peak

120 height of the first SRF measurement. In addition, it was verified by re-running the analysis (see Sect. 4.2) with several different SRFs measured throughout the campaign that changing the SRF used in the retrieval leads to changes of the result for the vertical column density (VCD) of NO_2 of up to 0.75%, which is much smaller than the overall retrieval error between 2% and 14% (depending on weather conditions). This leads to the conclusion that the grating spectrometer remained stable throughout the deployment. Since the remarkable ensemble performance of DOAS instruments was already demonstrated, e.g., in Piters

125 et al. (2012), and the stability and high accuracy of QE Pro spectrometers were demonstrated during long-term ground-based (Grossmann et al., 2018) deployments, as well as during aircraft-based (Stutz et al., 2017) and balloonborne measurements (Voss et al., 2024), additional performance tests, as done for the FTS (see Sec. 4.3), are not needed for this instrument.

2.3 Remote access

During previous campaigns, the instrument required an operator onboard the vessel (e.g., Butz et al. (2022)). For the present

130 campaign, the instrument was upgraded to operate fully automatically and to allow for remote access. To this end, custom-built software packages were used to automatically operate the two spectrometers, the temperature stabilization, all ancillary sensors, and the solar tracker. A maintenance crew only needed to go on board the vessel approximately every six weeks to exchange the hard drives used to store the data and to perform characterization measurements. In order to allow for remote access for quick instrument checks and to notify the maintenance crew in case of instrument errors, access via the mobile

135 phone network using an MC Technologies MC100 network switch with a Quectel EG21-1 module was installed. A 1.5 m long 790-960 MHz multiband antenna from MC Technologies with 6 dBi antenna gain was mounted on the ship's railing. Since the ship was traveling along the coast of Japan (see Sect. 3), this antenna was large enough to connect to the instrument on about 80% of the route.

3 Campaign overview

140 The vehicle carrier *Nichiyu Maru* offered the opportunity to test our setup with rather short lead times within the framework of the Ship of Opportunity (SOOP, https://www.soop.jp/) program by the National Institute for Environmental Studies (NIES). The ship travels along the coast of Japan, having a weekly round-trip schedule. This makes it possible to probe the emissions of
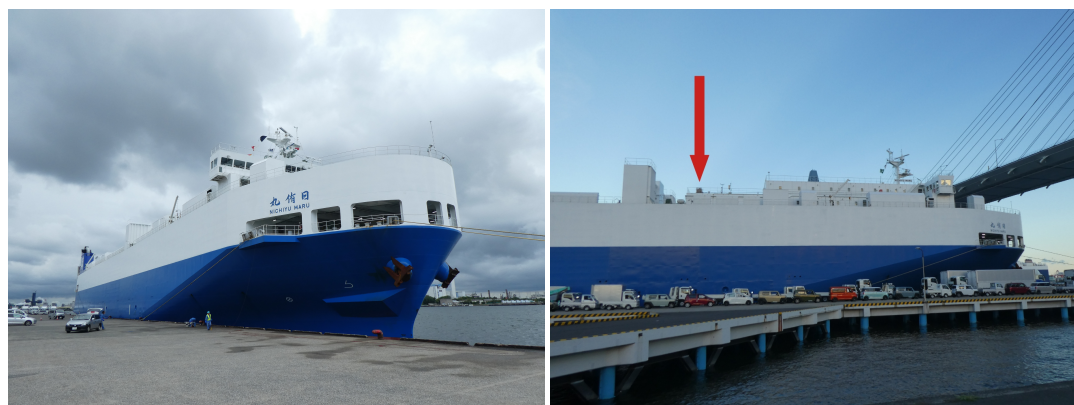
Figure 3. The vehicle carrier *Nichiyu Maru* (Ocean Link, Ltd.) (left) and the location of the instrument on the ship (right). The instrument is marked with a red arrow.

major industrial areas of Japan up to twice per week, depending on weather conditions. The *Nichiyu Maru* is therefore an ideal platform to test the use of our instrument for emission monitoring. In addition, the route of the *Nichiyu Maru* allows for easy

145 access since remote monitoring via the mobile phone network is possible (see Sect. 2.3) and maintenance access in a harbor close to NIES is possible once per week if needed. Finally, in situ data from the other instruments on board the *Nichiyu Maru* within the framework of SOOP is available, paving the way for future multi-instrument studies.

The *Nichiyu Maru* (Fig. 3), owned by Ocean Link, Ltd., is 160 m long, 25 m wide, and was built in 2019 (Nippon Kaiji Kyokai, 2024). Our instrumentation was installed on board the *Nichiyu Maru* (Fig. 1) from 16 September to 16 December 2023 and

150 from 17 February to 22 May 2024. Between the two periods, the ship was in the dry dock for maintenance. The instruments were positioned on the ship's upper deck at the location behind the bridge marked with the red arrow in Fig. 3. Care was taken to choose a location far away and in front of the chimney to prevent the ship's exhaust plume from interfering with the measurements. Indeed, no plume signatures were found in the spectra recorded while the ship was moving. The instrument's location corresponds to an average altitude between 27 and 30 m above sea level (as measured by the GPS sensor of the

155 instrument), depending on how heavily the *Nichiyu Maru* was loaded.

During the deployment described here, the *Nichiyu Maru* traveled along the east coast of Japan from the port of Kawasaki (Bay of Tokyo) to the port of Kanda (Fukuoka prefecture) and back once per week. It usually stopped at the ports of Nagoya, Sakaide (Takamatsu prefecture), Kurashiki (Okayama prefecture), and Hiroshima on the way from Kawasaki to Kanda, and at the ports of Kurashiki (Okayama prefecture), Toyohashi (Aichi prefecture), and Yokosuka (Bay of Tokyo) on the way back to

160 Kawasaki. Additional stops occurred during some round trips in spring 2024, e.g., in Kobe (Hyogo prefecture). Although the *Nichiyu Maru* often is moored in the harbors during the day to load and unload vehicles and mostly sails at night, we were able to collect daytime measurements in the Seto Sea between Kitakyushu and Osaka, in the Nagoya region, and in the Bay of Tokyo (see Fig. 4) that allow for technical testing and for showcasing source attribution.
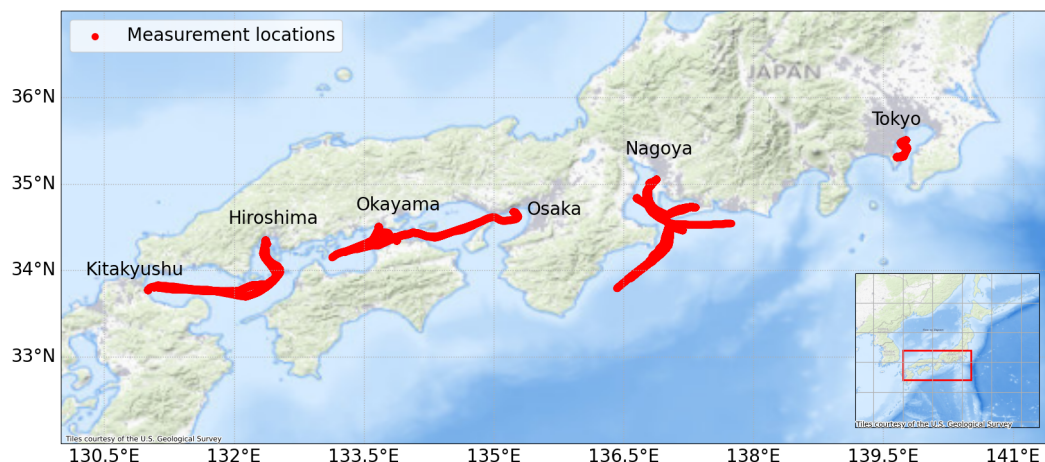
Figure 4. Locations (red) of the columnar measurements collected onboard the vessel *Nichiyu Maru* between September 2023 and May 2024.

4 Retrieval and data quality assurance

165 The retrieval procedure for CO_2, CH_4, and CO from EM27/SUN observations is described in Sect. 4.1 mostly following previous work (Klappenbach et al., 2015; Knapp et al., 2021; Butz et al., 2022). The retrieval of NO_2 from observations of the DOAS instrument is described in Sect. 4.2 following the DOAS principles (Platt and Stutz, 2008).

4.1 Retrieval of CO_2, CH_4, and CO from EM27/SUN measurements

In a first step, the interferograms recorded by the EM27/SUN FTS need to be Fourier transformed into spectra. To this end, as
170 in our previous work, the preprocessor of the PROFFAST retrieval software (Hase, 2000; Frey et al., 2021) is used, which is also employed for EM27/SUN data processing within the COCCON network (Frey et al., 2019). We use a spectral window of 3500 to 14000 cm^{-1} for channel 1 and 3000 to 5200 cm^{-1} for channel 2 of the FTS, a Mertz (1967) phase correction, and a Norton-Beer medium apodization (Norton and Beer, 1976, 1977) throughout this study. Before the Fourier transform, the direct current (DC) component of the interferograms is used to filter out scenes with low brightness or large brightness fluctuations
175 following Klappenbach et al. (2015) and Butz et al. (2022). Large brightness fluctuations indicate clouds passing by or the tracker not fully compensating for the ship's motion. Following Knapp et al. (2021), the DC-variability of an interferogram can be defined as

$$DC_{var} = \frac{\max(I_{DC})}{\min(I_{DC})} - 1 \tag{1}$$

where I_{DC} is the intensity of the DC-component of the interferogram. All interferograms with a DC-variability greater than 5%
180 throughout the integration time of the measurement are filtered out. In addition, a low average DC value can indicate clouds passing in front of the sun. Therefore, interferograms with an average DC value lower than 5% are excluded from any further

	Window 1	Window 2	Window 3	Window 4	Window 5	Window 6
Channel	1	1	1	1	1	2
Lower boundary [cm^{-1}]	7765	6308	6173	6030	5897	4210
Upper boundary [cm^{-1}]	8005	6390	6276	6145	6030	4320
Target absorbers	O_2	CO_2	CO_2	CH_4	CH_4	CO
Interfering absorbers	H_2O, O_2O_2	H_2O	H_2O	CO_2, H_2O	CO_2, H_2O	CH_4, H_2O

Table 2. Spectral windows and respective absorbing gases for the EM27/SUN measurements.

analysis.

The algorithm RemoTeC (Butz et al., 2011) performs the actual spectral retrieval. It was chosen here since the standard algorithm of the COCCON network, PROFFAST, currently does not accept moving instruments. The RemoTeC algorithm was

185 originally developed for the retrieval of gas abundances from the GOSAT satellite (Butz et al., 2011) but has since been applied to various satellites, including OCO-2 (Wu et al., 2018) and TROPOMI (Hu et al., 2016). Adapted versions for ground-based applications exist and have been applied to a variety of settings (e.g., Klappenbach et al. (2015), Luther et al. (2019), Knapp et al. (2021), and Löw et al. (2023)). For ground-based direct sun applications, RemoTeC neglects scattering, reducing the radiative transfer equation to Beer-Lambert's law. A priori profiles for the retrieval are calculated based on meteorological

190 data from NCEP (National Centers for Environmental Prediction et al., 2000), in situ ground-based pressure and temperature measurements, standard profiles for CH_4 and CO_2 from tracer model 4 (TM4) (Dentener et al., 2003; Meirink et al., 2006) and CarbonTracker (Peters et al., 2007) as well as standard profiles for CO based on tracer model 5 (TM5) (Huijnen et al., 2010). Spectral line parameters are taken from HITRAN 2016 (Gordon et al., 2017). The solar top-of-the-atmosphere reference spectrum is provided by G. Toon (2016, personal communication).

195 Formally, RemoTeC retrieves partial column densities for six altitude layers, which are equidistant in pressure, employing a Phillips-Tikhonov regularization scheme (Phillips, 1962; Tikhonov, 1963). Each target species' vertical column density (VCD) is then calculated by summing up the partial columns in these six layers. The forward model itself is calculated for 72 atmospheric layers based on Voigt line shapes. The forward model convolves the line-by-line spectra by the instrument SRF (often also called instrument lineshape (ILS) in the context of FTS) to simulate the observed spectra. The SRF was recorded on 23

200 August 2023, following the procedures of the COCCON protocol (Frey et al., 2015, 2019). Table 2 lists the spectral windows used for the retrieval of CO_2, CH_4, and CO as well as for molecular oxygen O_2. Water vapor H_2O is an interfering absorber. We use the retrieved O_2 and H_2O column densities to calculate the total pressure at the instrument level and call it 'spectroscopic' pressure p_{spec} since it is derived from spectroscopic measurements. For quality assurance, the spectroscopic pressure can be compared to the in situ surface pressure $p_{in\text{-}situ}$ measured by a co-deployed pressure sensor (cf. also Knapp et al. (2021)).

205 Deviations (on top of trivial offset factors between spectroscopic and in situ data) indicate potential error sources of our setup,

such as pointing errors of the solar tracker, drifts of the optical alignment, or spectroscopic parameter errors. Therefore, we use spectroscopic pressure as a quality filter as follows:

1. We remove outliers with $\left| 1 - \frac{p_{\text{spec}}}{p_{\text{in-situ}}} \right| < 0.05$.

2. Be R the average ratio $\frac{p_{\text{spec}}}{p_{\text{in-situ}}}$ over the entire campaign. We remove all data with $\left| 1 - \frac{p_{\text{spec}}}{p_{\text{in-situ}} \times R} \right| < 0.003$.

210 Further details on this filtering approach can be found in Klappenbach et al. (2015) and Knapp et al. (2021).

After filtering, the remaining VCDs of the absorbers are generated by averaging over ten consecutive retrievals to improve the signal-to-noise ratio and to make the dataset comparable to the COCCON standard (Frey et al., 2019). Averaging is stopped at a smaller number if gaps are detected. The column-average dry-air mole fractions X_{GAS} for a specific gas, from now on called mixing ratio, are calculated through

$$215 \quad X_{\text{GAS}} = \frac{\text{VCD}_{\text{GAS}}}{\text{VCD}_{\text{O}_2}} \times 0.2095 \tag{2}$$

(Wunch et al., 2011). Based on the side-by-side measurements described in Sect. 4.3, the VCDs and X_{GAS} are multiplied by a scaling factor such that they correspond to the ones measured by the TCCON station in Tsukuba (see Table 6). Finally, as recommended by Wunch et al. (2011), an empirical correction for a spurious airmass-dependent bias is applied as follows:

$$Z_{\text{GAS,corr}}(\Theta) = \frac{Z_{\text{GAS}}(\Theta)}{a\Theta^3 + b\Theta + c} \tag{3}$$

220 where Z is either a mixing ratio or a VCD, Θ is the SZA, and a, b, and c are empirically determined coefficients. These coefficients are based on measurements from Knapp et al. (2021), who previously used the same instrument for background measurements over the Pacific Ocean. It should be pointed out that this correction is applied to mixing ratios and VCDs separately, since the VCDs are later used to calculate enhancement ratios with respect to NO_2 VCDs, and the airmass-dependent bias is different in the O_2 and in the target gas retrieval windows.

225 **4.2 Retrieval of NO_2 from DOAS measurements**

Since, in contrast to CO_2 or CH_4 absorption in the near-infrared, absorption optical thicknesses of NO_2 are typically minor in the visible spectral range, we can apply the DOAS technique (Platt and Stutz, 2008) to infer NO_2 column densities from the measurements of the VIS spectrometer. The DOAS retrieval consists of several steps. A dark current, offset, and non-linearity correction is performed during preprocessing. Dark current and offset spectra are measured every night at 2 a.m. local 230 time throughout the campaign and are then used for the respective correction. A non-linearity correction is performed using a ninth-degree polynomial, which was determined in the laboratory based on measurements of a halogen light source recorded at various exposures. Afterwards, typically 100 spectra are co-added. The co-addition is stopped at less than 100 spectra if the exposure time changes, the spectra have a saturation of less than 8% (which is typical for measurements during sunrise and sunset or during the presence of larger clouds), large saturation fluctuations are detected (which relates to perturbed sun-tracking), the 235 time between two subsequent spectra is longer than 70 seconds, or spectra are missing between subsequent measurements. All

Parameter	Setting
Fitting interval	433-485 nm
Baseline polynomial	3rd order
Intensity offset polynomial	1st order
Orthobase order	2
Shift & Stretch	1st order for reference, spectrum, Ring, and CLD
Absorbers/Pseudo-absorbers	NO_2 at 294 K, O_3, O_4, H_2O, IO, Ring, CLD, NO_2 at 220 K (orthogonalized to NO_2 at 294 K)
I_0-effect included in	NO_2, O_3, NO_2 at 220 K
Fraunhofer spectrum	Chance and Kurucz (2010)
SRF	450 nm krypton peak; recorded on 14 September 2023

Table 3. Parameters of the DOAS fit.

Absorber/Pseudo-absorber	Cross-section and temperature
NO_2	Vandaele et al. (1998), 294 K
O_3	Serdyuchenko et al. (2014), 243 K
O_4	Thalman and Volkamer (2013), 293 K
H_2O	Rothman et al. (2009), 293 K
IO	Spietz (2005), 298 K
NO_2, 220 K	Vandaele et al. (1998), 220 K
Ring	Based on Chance and Kurucz (2010)
CLD	Based on Neckel (1987) and the method by Bösch et al. (2003)

Table 4. List of absorption cross-sections and pseudo-cross-sections used in the DOAS retrieval.

co-added spectra consisting of fewer than 50 measurements are discarded.

After the preprocessing, the DOAS fit is performed using the software package QDOAS (Danckaert et al., 2017). QDOAS recalibrates the initial pixel-to-wavelength mapping based on the solar Fraunhofer lines as a first step. Then, the actual DOAS fit, based on Beer-Lambert's law, finds the differential slant column densities (dSCDs) of NO_2 and interfering absorbing gases together with ancillary parameters such as spectral shifts, a background polynomial, an intensity offset parameter accounting for instrument straylight, as well as a center-to-limb-darkening (CLD) and Ring effect correction required for direct-sun measurements in the presence of scattering due to high-altitude clouds. The latter is a typical weather condition during the deployment of the instrument. All DOAS fit parameters are detailed in Table 3, and a list of all absorption cross-sections used can be found in Table 4.

One of the key aspects of DOAS is that the retrieval finds dSCDs with respect to a reference spectrum I_0 measured by the very same spectrometer. In our case, this reference spectrum, taken for the entire campaign dataset, is recorded around noon under minimal airmass and cloud-free conditions on 17 October 2023. To get the total slant column densities (SCDs) throughout
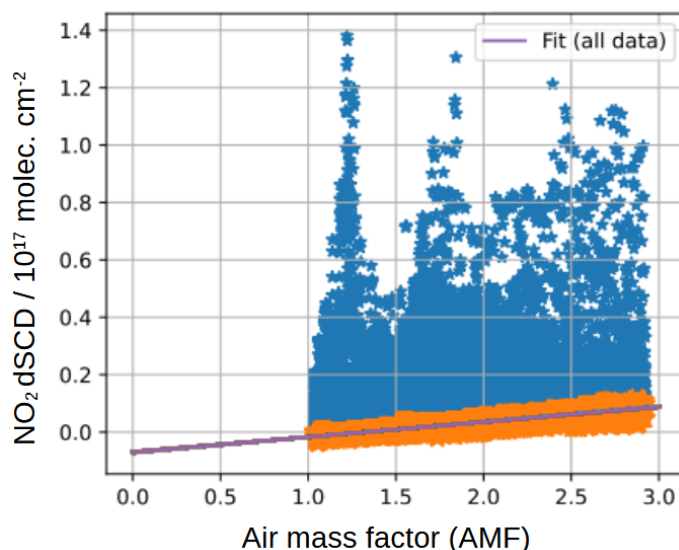
Figure 5. NO$_2$ Langley plot for the entire campaign dataset. Orange dots indicate background conditions used for finding SCD$_{ref}$. The purple line is the linear fit to all background data. The width of the purple line represents the ensemble of all bootstrap realizations used to calculate the error of SCD$_{ref}$.

the atmosphere, we need to add the absorber slant column density contained in the reference spectrum SCD$_{ref}$ to the dSCDs found by the DOAS fit. To find SCD$_{ref}$, we use an approach similar to the procedures of the PANDONIA network (Herman
250   et al., 2009) and the bootstrap method by Cede et al. (2006). The approach builds on Langley's method (Langley, 1904), which assumes the following linear relation for absorber i

$$dSCD_i = VCD_i \times AMF_i - SCD_{ref} \tag{4}$$

where AMF$_i$ is the air-mass factor, which can be approximated as $AMF = \frac{1}{\cos\Theta}$ as long as SZA $\Theta < 70°$ (Platt and Stutz, 2008). Thus, SCD$_{ref}$ is the ordinate intercept of a plot of the dSCDs versus the AMF.
255   Langley's method is only applicable for background measurements where the gas concentrations do not change over the range of SZA used for the plot, i.e., over the course of a day. Since our NO$_2$ measurements are conducted in the vicinity of local NO$_2$ sources and NO$_2$ is variable due to photochemistry and meteorological transport, our measurements do not fully comply with this assumption. However, since we use a single reference spectrum for the entire campaign period, we can assemble a composite Langley plot for NO$_2$ spanning many days as shown in Fig. 5. The composite Langley plot reveals a sharp, well-defined
260   lower boundary, defined by background conditions composed of many individual days. To find SCD$_{ref}$, we define background conditions as the 20% lowest dSCDs in each 0.1 AMF bin (orange data in Fig. 5) and fit the linear relationship given by Eq. 4 to this background data. For uncertainty estimation, we use a bootstrap method, repeating the fit procedure multiple times with randomly chosen subsets of the background data and taking the maximum and minimum of the found SCD$_{ref}$ as the error range.

The error introduced by arbitrarily choosing 20% as a threshold was estimated by re-running the whole analysis with different thresholds between 5% and 40%. The total error is then the Gaussian sum of the error of the bootstrap realizations (0.51×10^{15} molec. cm^{-2}) and the error determined by changing the threshold (0.68×10^{15} molec. cm^{-2}). Based on this method, we find $SCD_{ref} = (-7.02 \pm 0.85) \times 10^{15}$ molec. cm^{-2} for NO_2, which is used to calculate total SCDs and together with the AMF the respective VCDs of NO_2.

Finally, quality filtering is applied to the NO_2 VCDs. Measurements with SZA>70° are filtered out since the cosine approximation used to calculate the AMF is not valid due to Earth's curvature becoming non-negligible (Platt and Stutz, 2008). Also, all measurements with a root-mean-square spectral fitting error (RMSE) of more than five times the average RMSE of the respective measurement day are discarded since a large RMSE indicates brightness fluctuations during the measurement, e.g., caused by variable cloud cover disturbing the solar tracking. Finally, for calculating ratios with respect to gases measured by the EM27/SUN, the NO_2 VCDs are also downsampled to the frequency of the EM27/SUN measurements by averaging the DOAS measurements to the time intervals of the EM27/SUN dataset.

4.3 Performance of the EM27/SUN spectrometer and comparison to instruments of the COCCON network

Shipborne deployments are a major challenge for FTS. Especially shocks during the transport of the instrument to the ship or constant vibrations on board, e.g., caused by the engine of the ship, may lead to misalignments or instrumental drift. For future operation of our instrument, for example, within the COCCON, it is crucial to verify that it remains stable throughout the deployment and can be operated within the error margin of land-based spectrometers. The important criteria for benchmarking the stability of an EM27/SUN FTS are the change of the spectral response function (SRF, often also referred to as instrument line shape (ILS)) and the drift of the spectrometer with respect to an instrument of a high-resolution, ground-based FTS network such as the Total Column Carbon Observing Network (TCCON). These two criteria were monitored throughout the deployment and are discussed in the following.

SRF measurements with the FTS were conducted before and after the deployment, as well as during the ship's maintenance break. These measurements were conducted following the procedure described in Frey et al. (2015) under controlled laboratory conditions. SRF measurements are impossible on the ship itself since the lamp assembly cannot be reliably set up onboard. All SRF measurements are evaluated with the retrieval software LINEFIT 14.6 (Hase, 2000) as described in Frey et al. (2015) and Frey et al. (2019) to be consistent with SRF measurements from previous campaigns.

Panels a and c of Fig. 6 show the modulation efficiency (ME) and the phase error (PE), respectively, of all SRF measurements conducted during the current deployment with the FTS. Since the instrument was not re-aligned since 2019, previous SRF measurements already reported in Knapp et al. (2021) and Hanft (2021), as well as previously unpublished SRF results from a deployment in 2022, are included in the figure. It should be noted that an abrupt SRF change reported in Knapp et al. (2021), which was at that time attributed to a shock during the transport from Heidelberg to Vancouver, was, in the meantime, attributed to a malfunction of the ancillary humidity sensor. After correction of this malfunction, the previously reported change disappears, as can be seen in Fig. 6.

During the current, latest deployment, our instrument has a ME of 0.9908 ± 0.0023 and a PE of 0.0013 ± 0.0013. If the whole
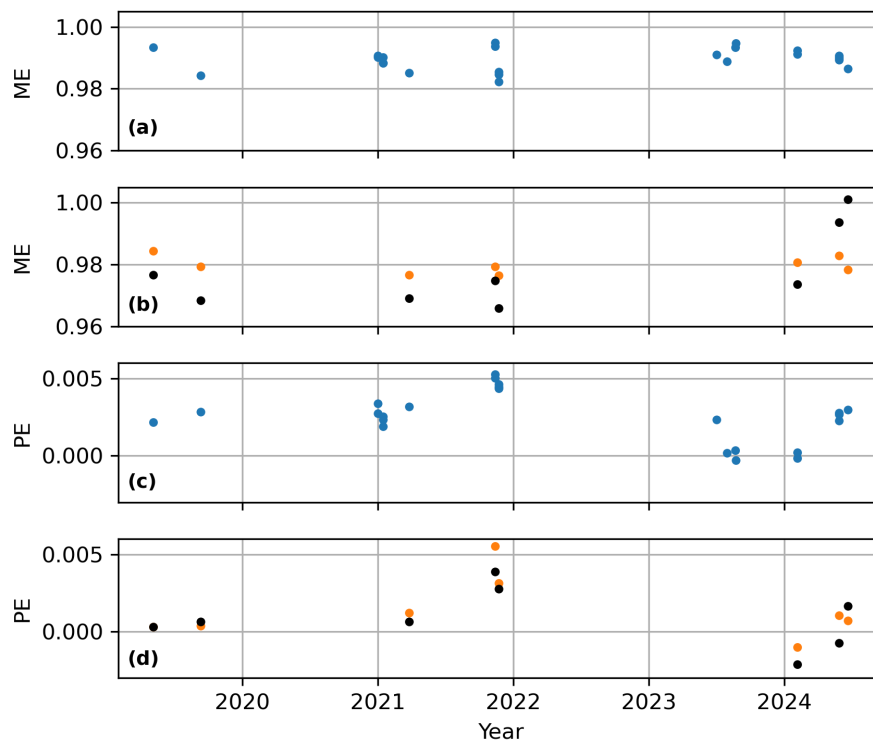
Figure 6. Overview of all spectral response function (SRF) measurements for the FTS conducted under controlled conditions in the laboratory since 2019. Panels a and c show the modulation efficiency (ME) and the phase error (PE), respectively, for an SRF retrieved based on the water vapor absorption lines in the spectral region between 7000 and 7400 cm^{-1} as used in the standard retrieval procedure described in Frey et al. (2015). Panels b and d show ME and PE retrieved based on the water vapor absorption in the overlap region between the two detectors (5275-5400 cm^{-1}) as recommended by Alberti et al. (2022). Orange dots are results from detector channel 1 (used to retrieve CO_2 and CH_4). Black dots are results from detector channel 2 (used to retrieve CO).

data since 2019 is considered, our instrument has a ME of 0.9895 ± 0.0034 and a PE of 0.0025 ± 0.0016. These numbers for ME and PE and the respective errors are similar to those reported by Herkommer et al. (2024) for the COCCON travel standard (ME: 0.9805 ± 0.0027, PE: -0.0020 ± 0.0006) and the reference instrument SN-37 of the COCCON network (ME: 0.9836 ± 0.0027, PE: 0.0015 ± 0.0012). Our results for ME and PE are also within the range known from other COCCON instruments as reported by Alberti et al. (2022), and our standard deviation for ME for the current campaign is smaller than the error budget of 0.29% derived by Frey et al. (2019) for the SRF retrieval procedure used in our study. Based on this, we conclude that despite frequent transports by aircraft and potential rough handling during craning, the SRF of our instrument has remained stable, and its changes are within the error margin of other instruments in the COCCON network. Thus, the same SRF measurement is used to evaluate the whole deployment (see Sect. 4.1).

As recommended by Alberti et al. (2022), the SRF of the second channel used for the retrieval of CO is also evaluated and

Date	Location	XCO_2	XCH_4	XCO	O_2	CO_2	CH_4	CO
28 October 2023	Kawasaki	1.0273	1.0262	1.0463	0.9794	1.0040	1.0128	1.0572
13 February 2024	Tsukuba	1.0284	1.0282	1.0402	0.9804	1.0027	1.0129	1.0378
14 February 2024	Tsukuba	1.0286	1.0254	1.0640	0.9807	1.0028	1.0100	1.0566
13 April 2024	Kawasaki	1.0296	1.0285	1.0273	0.9806	1.0046	1.0136	1.0225
15 May 2024	Kawasaki	1.0293	1.0285	1.0365	0.9784	1.0046	1.0126	1.0235
4 June 2024	Tsukuba	1.0284	1.0261	1.0845	0.9794	1.0034	1.0091	1.0529
5 June 2024	Tsukuba	1.0289	1.0264	1.0876	0.9787	1.0027	1.0083	1.0519
Mean	-	1.0287	1.0269	1.0591	0.9796	1.0035	1.0108	1.0427
Standard deviation	-	0.0006	0.0012	0.0231	0.0008	0.0008	0.0023	0.0132

Table 5. Scaling factors of X_{GAS} and VCDs measured by the shipborne EM27/SUN and the COCCON instrument (SN-147) during side-by-side measurements. The table lists the daily average ratios calculated as the COCCON data divided by the data from the shipborne instrument. Side-by-side measurements took place in Kawasaki harbor and at NIES in Tsukuba.

compared to a SRF retrieval from the main detector channel based on water vapor absorption in the 5275 to 5400 cm^{-1} spectral window, where both detectors are sensitive. The results are shown in panels b and d of Fig. 6. The deviations between the ME

310 and the PE of the two channels of our EM27/SUN are similar to those reported by Alberti et al. (2022) for other instruments of the COCCON network. In addition, changes between the different measurements are similar to those for the standard SRF retrieval shown in panels a and c of Fig. 6. Only in May 2024, the ME of channel 2 (black dots in Fig. 6) is found somewhat higher than before and is also higher than the ME for detector channel 1, in contrast to previous measurements, but the change is still within the range of deviations reported from other COCCON instruments (Alberti et al., 2022).

315 In addition to monitoring the SRF, our instrument has been regularly compared to an instrument of the COCCON network (SN-147). Roughly every six weeks, we operated the two instruments side-by-side in the harbor of Kawasaki (Tokyo metropolitan area). For this, both EM27/SUN instruments were placed on the deck of the vessel *Nichiyu Maru*. Additional comparison measurements in the courtyard of NIES in Tsukuba were performed before and after the campaign, as well as during a maintenance break in February 2024. The COCCON instrument itself is regularly compared to the TCCON station in Tsukuba (Ohyama

320 et al., 2009) to ensure a good quality of the COCCON instrument.

To evaluate the stability of our EM27/SUN with respect to the COCCON instrument, average ratios between the two instruments are calculated for the VCDs and X_{GAS} for all individual days when side-by-side measurements were conducted. The data reduction for measurements of the shipborne EM27/SUN follows Sect. 4.1. The measurements of the COCCON instrument are processed according to the standard COCCON protocol (Frey et al., 2019), relying on the retrieval software

325 PROFFAST. Table 5 lists the daily ratios between the gas retrievals from the COCCON measurements and those of the shipborne EM27/SUN. Based on the seven comparison days, average ratios of 1.0287 ± 0.0006 for XCO_2, 1.0269 ± 0.0012 for XCH_4, and of 1.0591 ± 0.0231 for XCO are found. The overall ratios are larger than the ones between different COCCON instruments reported by Alberti et al. (2022), which is related to differences in RemoTeC and PROFFAST. Most importantly,

XCO_2	1.0275 ± 0.0019
XCH_4	1.0252 ± 0.0019
XCO	1.0945 ± 0.0391
CO_2	1.0229 ± 0.0023
CH_4	1.0139 ± 0.0027
CO	1.1129 ± 0.0342
O_2	0.9812 ± 0.0024

Table 6. Overall scaling factors applied to X_{GAS} and VCDs retrieved from the shipborne EM27/SUN measurements to make them consistent with the TCCON measurements in Tsukuba.

PROFFAST corrects for a spectroscopic error in the O_2-column, which accounts for a bias of about 2% (Wunch et al., 2010),
330 and has already an overall scaling factor with respect to TCCON included, while RemoTeC leaves these corrections to the post-processing. A correction for the difference between RemoTeC and PROFFAST is later applied through an overall scaling factor with respect to TCCON in the retrieval as described in Sect. 4.1.

Inter-day differences are small for XCO_2 and XCH_4 as well as for the VCDs of O_2, CO_2, and CH_4, as can be inferred from the standard deviations listed in Table 5. Inter-day differences are larger for XCO and the VCDs of CO, but the overall accuracy
335 and precision requirement is much less stringent than for CO_2 and CH_4. For CO, intra-day differences show an SZA dependency on the same order of magnitude as the inter-day variability.

Our standard deviations for XCO_2 and XCH_4 listed in Table 5 have a similar order of magnitude as the ones reported by Frey et al. (2019) for the reference instrument of COCCON with respect to TCCON (0.0015 for XCO_2, 0.0024 for XCH_4), which are, however, based on data from a much longer time series. Thus, our assessment suggests that our shipborne EM27/SUN
340 complies with the standards of the COCCON network. The overall scaling factors for our instrument with respect to TCCON were calculated by multiplying our scaling factors from the comparison measurement in Kawasaki on 28 October 2023 with average scaling factors from comparison measurements between the COCCON instrument and the TCCON station in Tsukuba made in 2023 (see Table 6). The TCCON data is retrieved with the standard GGG2020 algorithm (Laughner et al., 2024).

5 Observing emission patterns in Mikawa Bay, Nagoya region

345 To demonstrate the potential of our shipborne instrument for characterizing fossil emission sources selectively, we examine measurements collected on 13 November 2023, when the ship was crossing Mikawa Bay, which is part of the greater Nagoya region. We selected this period as it showcases the main advantages of the multi-species setup to selectively determine emission plumes of different sources. The greater Nagoya region is an ideal location for such a study since the city of Nagoya, northwest of Mikawa Bay, is among the largest urban centers, and, after Tokyo, Yokohama, and Osaka, the fourth largest agglomeration
350 in Japan (Statistics Bureau of Japan, 2020). The greater Nagoya region is characterized by many large point sources such as large coal-, gas-, and oil-fired power plants, one of Japan's largest steel factories, and refineries (Climate TRACE coalition,
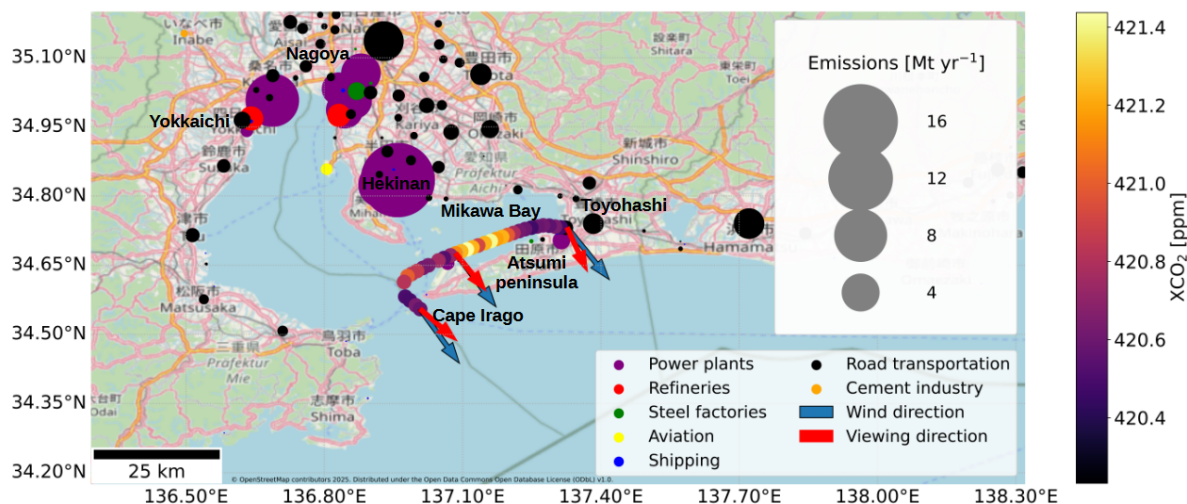
Figure 7. Overview of the case study in Mikawa Bay on 13 November 2023. The ship's trajectory from Toyohashi to Cape Irago is illustrated through color coding of the XCO_2 measurements collected by the shipborne EM27/SUN. The blue arrows indicate the wind directions taken from ERA-5 (Hersbach et al., 2020) interpolated to the location of the measurement for each hour, while the red arrows indicate the viewing direction towards the sun. The circles of variable size and color illustrate CO_2 point sources, where the circle size corresponds to emission rates and color to the type of the emission sources according to Climate TRACE coalition (2022). See legends for details.

2022). In addition, traffic and shipping are significant sources of anthropogenic emissions.

Figure 7 shows the study region and the ship track. The ship *Nichiyu Maru* left Toyohashi port (Aichi prefecture) at 13:05 Japan Standard Time (JST), traveled westward along the coast of the Atsumi peninsula through Mikawa Bay, and rounded Cape Irago
355 towards the open ocean at around 14:50 JST. After 14:50 JST, no data is available due to changing weather conditions. During the transect through Mikawa Bay, the ship was downwind of the emission sources from the greater Nagoya region, which are also shown in the figure.

Figure 8 shows the time series of XCO_2, XCH_4, XCO, and the NO_2 VCDs. The mixing ratios of CO_2, CO, and the VCD of NO_2 shown in panels a, c, and d have a general increase during the observed period. Distinct peaks are visible in the time series
360 for XCO_2, XCO, and NO_2 VCDs, with sharp increases of 0.75 ppm, 0.015 ppm, and 0.5×10^{16} molec. cm^{-2}, respectively, between 13:30 and 14:00 JST. During that period, XCO_2 shows two distinct peaks at 13:40 and 13:50 JST, while XCO and NO_2 show only the first peak clearly. Other small increases are observed between 14:15 and 14:30 JST, and for NO_2 at 13:15 JST. XCH_4 shown in panel b of Fig. 8 shows a general downward trend with distinct peaks and is not regarded further.

To investigate the underlying emission patterns for the plumes between 13:30 and 14:00 JST, we calculate enhancements Δ
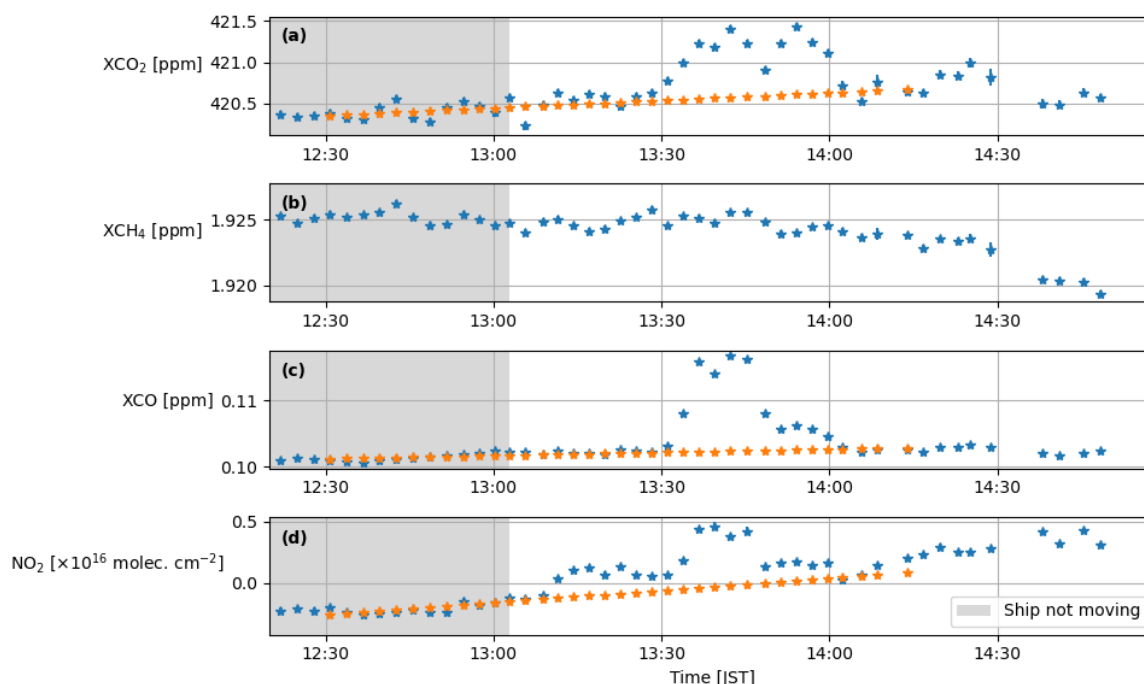
Figure 8. Time series of XCO$_2$ (panel a), XCH$_4$ (panel b), XCO (panel c), and NO$_2$ (panel d) measured on 13 November 2023 across Mikawa Bay. The estimated background level for the two major plumes is plotted in orange. During the grey-shaded period in the beginning, the ship was in the harbor of Toyohashi.

365 of each species and their enhancement ratios. For this purpose, we remove the background concentrations and convert NO$_2$ to NO$_x$ to make our results comparable with inventory data and standard emission ratios.

For background removal, we fit a line to the measurements before and after the plume using a least-squares method. Care is taken to exclude from the fit measurements with other enhancements (e.g., in the NO$_2$ VCD between 13:10 and 13:20 JST). The background level defined by this method is shown in orange in Fig. 8.

370 To convert NO$_2$ to NO$_x$ (=NO+NO$_2$), we use a conversion factor of NO$_x$/NO$_2$= 1.32 taken from Beirle et al. (2019), where it has been derived based on the assumption of photostationary steady state. The reasoning in Beirle et al. (2019) and Beirle et al. (2021) suggests that this factor can be applied here, since our measurements are taken at sunny conditions with SZA<65°, the air masses inside the plume are generally polluted and near the surface, and the measurements are taken far enough from the source for the NO-to-NO$_2$ conversion inside the plume to be roughly in equilibrium. Additionally, Beirle et al. (2021) have

375 calculated the NO-to-NO$_2$ ratio for various global regions. The annual average for different regions in Japan between 1.25 and 1.45 is close to the global average of 1.32. Because of this, we use this factor in our study, although considerable uncertainties remain.

Figure 9 (panels a-c) shows the enhancements Δ of XCO$_2$, XCO, and NO$_x$. A clear separation between two distinct episodes
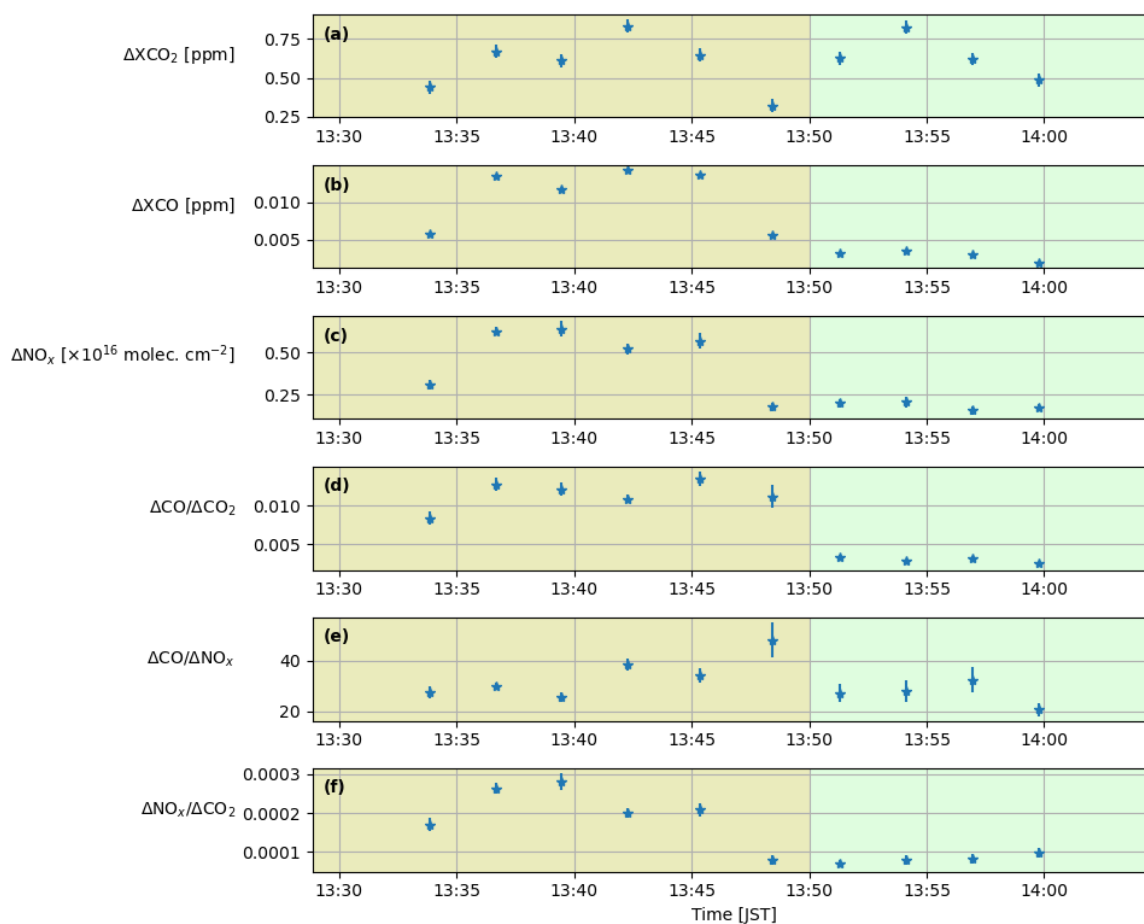
Figure 9. Panels a-c: Enhancements after the subtraction of the background (marked orange in Fig. 8) and trace gas ratios in the plumes measured on 13 November 2023. NO_2 has been converted to NO_x using the conversion factor of 1.32 from Beirle et al. (2019). Panels d-f: Enhancement ratios calculated based on the enhancements shown in panels a-c. The yellow and green background shading refers to episodes A and B as defined in the main text.

is seen with high values in ΔXCO and ΔNO_x before 13:50 JST (episode A, yellow shading in Fig. 9), and low concentrations

380 afterwards (episode B, green shading in Fig. 9). In contrast to this, during both episodes, ΔXCO_2 shows a distinct peak. This observation supports the existence of two different air masses with two different sources.

The distinct ΔXCO in episode A is much larger than all other CO enhancements detected throughout the transect (see Fig. 8). It requires a strong, local emitter upwind of the route of the *Nichiyu Maru*. Figure 10 compares the position of the measured CO-plume to three emission inventories: the Regional Emission inventory in ASia (REAS, version 3) compiled for the year

385 of 2015 (Kurokawa and Ohara, 2020) and two different versions of the Emissions Database for Global Atmospheric Research (EDGAR) compiled for 2018 and 2022 (Crippa et al., 2018, 2024). All three inventories contain a single grid cell with CO emissions being much larger than in all other grid cells. The main CO emission source of this grid cell is listed as "steel manufacturing" in the inventories. In the case of REAS (panel a) and EDGAR v8.1 (panel c), the location of the point source is upwind of the location where our instrument measured the largest enhancement. For EDGAR v6.1 (panel b), the large emitter

390 is displaced by roughly 0.3° longitude to the west, which tends to align worse with our measurements, considering the ERA-5 wind direction. The misplacement of the steel factory in EDGAR v6.1 was indeed confirmed by the EDGAR team (personal communication). This shows the capability of our setup to validate the correct positioning of point sources in inventories.

In order to delve deeper into the origin of the enhancements in episodes A and B shown in Fig. 9, we calculate enhancement ratios from our measurements to compare them to the emission ratios of inventory grid cells or source types. Each source

395 type emits a characteristic ratio of the trace gases CO_2, CO, and NO_x (see Table 7), which can be related to the fuel type as well as the type and efficiency of combustion. Concerning fuel type, for example, lignite coal contains, on average, more nitrogen, much less carbon, and much more oxygen than crude oil (Klemm and Hoppe, 1980), leading to a higher NO_x/CO_2-ratio for oil-fired compared to coal-fired power plants (Guevara et al., 2024). With respect to combustion efficiency, significant CO emissions are indicative of incomplete combustion (Klemm and Hoppe, 1980), which is typical for biomass burning or

400 steel factory blast furnaces (Zhong et al., 2017; Schneising et al., 2024). Finally, NO_x is also a combustion tracer formed by the highly temperature-dependent Zeldovich mechanism (Zeldovich, 1984) and is therefore indicative of the combustion temperature. The theoretically expected emission ratios are further altered through emission mitigation technologies such as selective catalytic reduction, which removes NO_x from power plant plumes (Srivastava et al., 2005), leading to characteristic emission signatures for different technologies. When comparing emission ratios to enhancement ratios in the atmosphere,

405 various emission contributions can blend due to atmospheric transport and mixing, such that the atmospheric enhancement has contributions from various emission sources.

In order to calculate enhancement ratios from our measurement, we convert the measured concentration enhancements (in units of vertical column densities (molec. cm^{-2})) into mass enhancements (in units of mass fractions or mass columns (kg cm^{-2})) using the molar mass of the respective species. Then we calculate mass ratios (in units kg kg^{-1}) to compare to the

410 reported emission ratios. The enhancement ratios measured with our instrument show large differences between the two plume episodes, as can be seen in panels d-f of Fig. 9 and Table 7 (upper rows). During episode A, $\Delta CO/\Delta CO_2$, $\Delta NO_x/\Delta CO_2$, and $\Delta CO/\Delta NO_x$ are on average larger than in episode B, suggesting that the emissions sources were different for the two episodes. In the following, both episodes are compared separately to the gridded EDGAR inventory and potential source signatures.
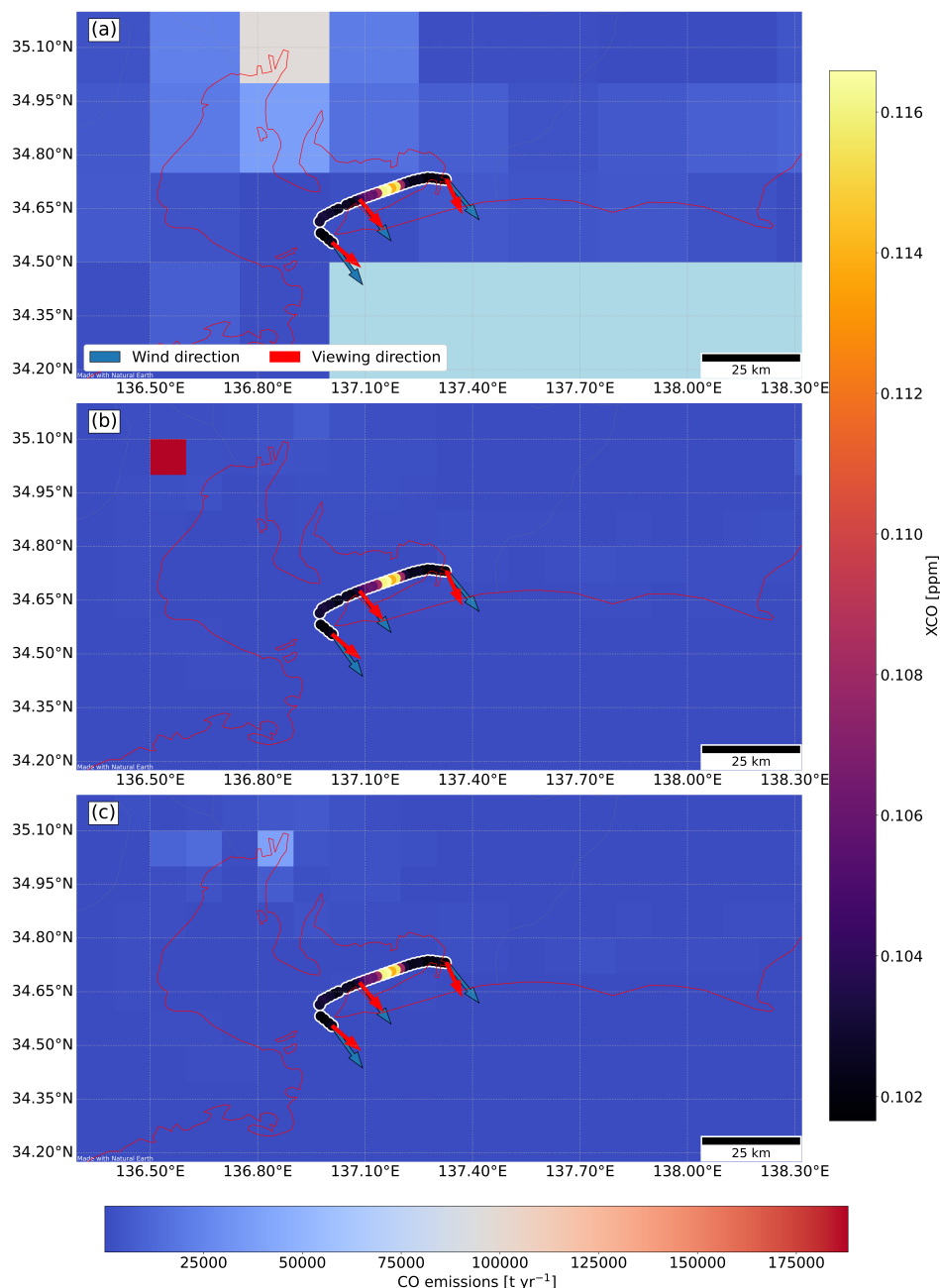
Figure 10. Comparison of measured XCO enhancements to CO emission patterns from different inventories: (a) REAS inventory for 2015 (Kurokawa and Ohara, 2020); (b) EDGAR v6.1 for 2018 (Crippa et al., 2018); (c) EDGAR v8.1 for 2022 (Crippa et al., 2024). Wind directions (blue arrows), interpolated to the location and time of the measurement, are taken from ERA-5 (Hersbach et al., 2020). Viewing direction is shown by the red arrows. Note that the REAS inventory (a) only includes land grid cells.

	$(\Delta)CO/(\Delta)CO_2$	$(\Delta)NO_x/(\Delta)CO_2$	$(\Delta)CO/(\Delta)NO_x$	Reference
Enhancement 1 (13:30-13:50)	$(8.0-14.0)\times10^{-3}$	$(1.8-3.0)\times10^{-4}$	$(25-60)$	Our measurement
Enhancement 2 (13:50-14:00)	$(2.5-4.5)\times10^{-3}$	$(7-10)\times10^{-5}$	$(20-30)$	Our measurement
EDGAR grid cells:				EDGAR inventory for 2022, v8.1
34.8°N/136.9°E (Hekinan power plant)	1.6×10^{-4}	5.4×10^{-4}	3.0×10^{-1}	
34.9°N/136.8°E (Nagoya refinery)	1.1×10^{-3}	1.1×10^{-3}	1.0	
35.0°N/136.8°E (Nagoya steel factory and harbor area)	1.7×10^{-3}	8.5×10^{-4}	2.0	
35.0°N/136.6°E (Yokkaichi power plant)	1.4×10^{-3}	5.2×10^{-4}	2.6	
34.9°N/136.6°E (Yokkaichi refinery and power plants)	1.0×10^{-3}	1.4×10^{-3}	7.1×10^{-1}	
Fuel / source type				
Bituminous coal	1.86×10^{-4}	8.40×10^{-4}	2.21×10^{-1}	Guevara et al. (2024)
Lignite	4.20×10^{-4}	9.39×10^{-4}	4.47×10^{-1}	Guevara et al. (2024)
Crude and fuel oil	3.76×10^{-4}	1.31×10^{-3}	2.87×10^{-1}	Guevara et al. (2024)
Diesel	3.48×10^{-4}	5.22×10^{-3}	6.66×10^{-2}	Guevara et al. (2024)
Natural gas	6.23×10^{-4}	1.20×10^{-3}	5.19×10^{-1}	Guevara et al. (2024)
Blast furnace	3.24×10^{-2}			Schneising et al. (2024)
			60-122	Van der Maas (2019)
Shaft kiln (cement)	7.50×10^{-2}	6.18×10^{-4}	121.29	Liu et al. (2021)
Other cement factories	9.18×10^{-3}	5.87×10^{-3}	1.30	Liu et al. (2021)
		2.69×10^{-3}		Brown et al. (2014)
EURO 5 vehicles:				Fontaras et al. (2014)
Urban, gasoline	5.00×10^{-3}	2.50×10^{-4}	20	
Urban, diesel	4.00×10^{-3}	1.34×10^{-3}	3	
Motorway, gasoline	6.67×10^{-3}	1.34×10^{-4}	50	
Motorway, diesel	1.34×10^{-4}	2.67×10^{-3}	5.00×10^{-2}	
Urban areas	$(0.01-3.30)\times10^{-3}$	$(0.07-10.50)\times10^{-5}$		Park et al. (2021)
Ships (transit)	2.33×10^{-3}	2.50×10^{-2}	9.31×10^{-2}	Kesgin and Vardar (2001)
Ships (port)			$(1.06-1.19)\times10^{-1}$	Zhao et al. (2022), Xiao et al. (2022)

Table 7. Overview of the measured enhancements (Δ), emission ratios for different fuel types and sources, and emission ratios taken from the EDGAR inventory (Janssens-Maenhout et al., 2019; Crippa et al., 2024) for the grid cells with the largest point source emitters in the studied region. Source types discussed in the text are marked in bold

The first plume meaured between 13:30 and 13:50 JST (episode A; yellow shading in Fig. 9) has a $\Delta CO/\Delta CO_2$ of (8.0-
415 14.0)$\times 10^{-3}$, a $\Delta CO/\Delta NO_x$ of 25-60 and a $\Delta NO_x/\Delta CO_2$ of (1.8-3.0)$\times 10^{-4}$. If this is compared to the emission ratios of the
EDGAR grid cells containing large emitters listed in the upper part of Table 7, the measured $\Delta NO_x/\Delta CO_2$ is found a factor 2
or more lower, and the measured $\Delta CO/\Delta CO_2$ as well as the measured $\Delta CO/\Delta NO_x$ are a factor 5 to 10 larger than the emission
ratios in all EDGAR grid cells.

As pointed out previously, the large CO content of the plume in episode A suggests a steel factory as the most likely source.
420 According to a new study based on satellite data (Schneising et al., 2024), blast furnace steel production can lead to CO/CO_2
emission ratios of 3.24×10^{-2} on average. Indeed, the Nippon Steel Nagoya factory operates two large blast furnaces and
two basic-oxygen furnaces (Nippon Steel Corporation, 2024). Also the large $\Delta CO/\Delta NO_x$ enhancement ratios are compatible
with emissions from steel factories (Van der Maas, 2019) (see also Table 7). For steel factories, Van der Maas (2019) found a
CO/NO_x emission ratio between 60 and 122 based on data from the TROPOMI satellite for five blast furnaces. They point out
425 that these findings disagree by up to one order of magnitude with the EDGAR v6.1 inventory (Crippa et al., 2018; Janssens-
Maenhout et al., 2019), which reports emission ratios between 2.8 and 16.8 for the same blast furnaces. This discrepancy is
partly attributed to EDGAR relying on end-of-pipe measurements at the chimney and not including fugitive emissions within
steel factories. Based on the emission ratios found by Van der Maas (2019) and Schneising et al. (2024), a blast furnace as the
major source would fit our measured enhancement ratio quite well.

430 Because of this, the enhancement ratios involving CO suggest the steel factory as the main source of plume episode A. In
addition, the low measured NO_x/CO_2 ratio might point at mixing of the plume with air masses carrying low NO_x/CO_2 ratios,
such as caused by traffic (2.5×10^{-4} (Fontaras et al., 2014), assuming EURO 5 engines, urban driving conditions, and a vehicle
fleet dominated by gasoline engines, which is typical for Japan (IEA-AMF, 2023)) or gas-fired power plants. Indeed, the city
center of Nagoya, with a high traffic density, and several gas-fired power plants are located in the vicinity of the steel factory
435 (Climate TRACE coalition, 2022). The latter are equipped with low-NOx burners or denitration equipment (Jera Corporation,
2025), which reduces the NO_x/CO_2 ratio of a gas-fired power plant listed in Table 7 by up to 90% (Crippa et al., 2018).
Although the EDGAR inventory at the grid cell level cannot fully explain the enhancement signature of episode A, a fitting
source composition dominated by steel factory emissions and contributions from gas-fired power plants with low-NOx burners
and traffic can be found based on the measured enhancement ratios.

440 Episode B (green shading in Fig. 9) of the plume detected after 13:50 JST contains much less CO and NO_x than episode A,
implying lower $\Delta CO/\Delta CO_2$ and $\Delta NO_x/\Delta CO_2$ enhancement ratios (see Table 7). This hints at a different source composition
than for episode A. From the approximate wind direction shown in Fig. 7, the coal-fired Hekinan power plant, one of the largest
in Japan (Climate TRACE coalition, 2022), and the two smaller co-located coal-fired power stations, Taketoyo and Nagoya,
appear to be likely sources. Other large emitters in the Nagoya region, such as the Yokkaichi power plant, are located upwind
445 of these three power plants as seen from the ship's position and may, therefore, also partly contribute.

Based on the EDGAR inventory (Crippa et al., 2024), the grid cell containing these three large coal-fired power plants should
have a CO/CO_2 emission ratio of 1.6×10^{-4}, a CO/NO_x emission ratio of 0.3, and a NO_x/CO_2 emission ratio of 5.4×10^{-4}.
The measured enhancement ratios $\Delta CO/\Delta CO_2$ of (2.5-4.5)$\times 10^{-3}$ and $\Delta CO/\Delta NO_x$ of 20-30 are however considerably larger

and the enhancement ratio $\Delta NO_x/\Delta CO_2$ of $(7\text{-}10)\times10^{-5}$ is considerably smaller than the respective emission ratios of the EDGAR grid cell containing the power plants. Part of the discrepancy between EDGAR and our measurement can, however, be explained by the Taketoyo power plant as well as one out of two units of the Nagoya power plant and three out of five units of the Hekinan power plant being switched off for maintenance or due to technical failures (Japan Electric Power Exchange, 2024). Because of this, other co-located sources with different emission ratios, such as traffic, are expected to contribute relatively more to the measured enhancement ratios. Therefore, our measurements are not expected to match the emission ratios from EDGAR. Indeed, the city center of Nagoya is located approximately upwind of our measurement from Hekinan. A study on urban emission ratios based on satellite data by Park et al. (2021) showed that urban areas of selected cities of different sizes in the northern hemisphere have emission signatures similar to our measured enhancement ratios (see Table 7). Episode B illustrates that while EDGAR and other inventories typically provide annual emission data, regular ship-based measurements can be used to inform on the temporal profiles of emissions and irregular emission behavior, such as shutdowns. This showcases the advantage of our instantaneous measurements, which can be used to infer irregular emission patterns, in contrast to the top-down approach of inventories such as EDGAR, relying solely on annual means.

The current study is limited by the approximate use of wind directions from the ERA-5 reanalysis (Hersbach et al., 2020). A higher accuracy in source attribution can be achieved by combining the data of our instrument with modelled airmass trajectories or footprints.

6 Conclusion and outlook

We have developed an autonomous multi-species mobile spectrometer setup consisting of an EM27/SUN FTS for the shortwave-infrared and a DOAS grating spectrometer for the visible wavelength range, both using direct sunlight as a light source. This setup has been successfully deployed and operated without permanent human attendance over several months on a commercial vessel traveling along the coast of Japan. The setup allows for measuring column abundances of CO_2, CH_4, CO, and NO_2 with high precision and repeatability. The latter has been tracked through regular side-by-side measurements with a spectrometer of the COCCON. This shows that our shipborne measurements of CO_2, CH_4, and CO are compatible with the standards of the COCCON and, in consequence, they can be adjusted to the TCCON scale through a multiplicative adjustment. Thus, our setup is suitable for satellite validation over the oceans. For a case study in the vicinity of Nagoya, we have demonstrated the detection of plume enhancements, ΔCO_2, ΔCO, and ΔNO_2, carrying the outflow from the heavily populated region. Converting ΔNO_2 into ΔNO_x under assumption of photochemical steady state, the enhancement ratios $\Delta CO/\Delta CO_2$, $\Delta NO_x/\Delta CO_2$, and $\Delta CO/\Delta NO_x$, together with wind information, suggest that the first episode of the plume originates mainly from a steel factory while the second episode most likely relates to emissions from coal-fired power plants and sources of urban signature. Comparing these findings to emission inventories such as EDGAR, we find that the gridded emissions and their ratios can be successfully checked using routine shipborne measurements. Due to the multi-species system, a source-sensitive assessment is feasible, which is especially valuable in regions of densely spaced emitters. Building on the demonstrated potential of the

instrument, long-term shipborne installations will enable routine satellite validation (on the open ocean), as well as systematic emission monitoring along coastal hotspots.

Code and data availability. Code and data are available from the authors upon request.

Author contributions. VE, RK, and MK developed the instrumental setup. KV supported the implementation of the DOAS spectrometer. FH
485 supported the technical developments and provided the PROFFAST software suite. VE, AM, MF, and RK deployed the instrument onboard the vessel and remotely operated the measurements. HT, HN, and SN led the deployment, and IM provided technical guidance. VE developed the data analysis framework and performed the data analysis. BL and KV supported the development of the data analysis framework and provided code. IM operated the TCCON station in Tsukuba and provided the TCCON data. SV provided guidance for the comparison to inventory data. AB developed the RemoTeC software, conceived and led the overall activity. VE wrote the first version of the manuscript; all
490 authors contributed to the final manuscript.

Competing interests. At least one of the (co-)authors is a member of the editorial board of Atmospheric Measurement Techniques. The authors declare no other competing interests.

Acknowledgements. The authors would like to acknowledge Tomoyasu Yamada and Eiji Yoshida (Global Environmental Forum (GEF)) for providing logistical and operational support for the instrument. In addition, the authors would like to thank Ocean Link Ltd. for the
495 possibility to operate an instrument onboard the vessel *Nichiyu Maru*. VE would like to acknowledge the work of Valentin Hanft and Nicolas Kai Neumann, who performed some of the SRF measurements included in Fig. 6. VE would like to acknowledge the use of the heiDOAS code package provided by Udo Frieß. The authors would like to acknowledge the EDGAR team for feedback on the source attribution. KIT acknowledges support by ESA for realizing COCCON activities through projects COCCON PROCEEDS (contract 4000121212/17/I-EF) and COCCON OPERA (contract 4000140431/23/I-DT-Ir). The operation of the Tsukuba TCCON site is supported in part by the GOSAT
500 series project. The SOOP program by NIES is financially supported by the Global Environmental Research Coordination System from the Ministry of the Environment of Japan (E1253, E1751, E1851, E1951, E2252, E2351). For the publication fee, we acknowledge financial support from Heidelberg University.

References

Alberti, C., Hase, F., Frey, M., Dubravica, D., Blumenstock, T., Dehn, A., Castracane, P., Surawicz, G., Harig, R., Baier, B. C., Bès, C., Bi, J., Boesch, H., Butz, A., Cai, Z., Chen, J., Crowell, S. M., Deutscher, N. M., Ene, D., Franklin, J. E., García, O., Griffith, D., Grouiez, B., Grutter, M., Hamdouni, A., Houweling, S., Humpage, N., Jacobs, N., Jeong, S., Joly, L., Jones, N. B., Jouglet, D., Kivi, R., Kleinschek, R., Lopez, M., Medeiros, D. J., Morino, I., Mostafavipak, N., Müller, A., Ohyama, H., Palmer, P. I., Pathakoti, M., Pollard, D. F., Raffalski, U., Ramonet, M., Ramsay, R., Sha, M. K., Shiomi, K., Simpson, W., Stremme, W., Sun, Y., Tanimoto, H., Té, Y., Tsidu, G. M., Velazco, V. A., Vogel, F., Watanabe, M., Wei, C., Wunch, D., Yamasoe, M., Zhang, L., and Orphal, J.: Improved calibration procedures for the EM27/SUN spectrometers of the COllaborative Carbon Column Observing Network (COCCON), Atmospheric Measurement Techniques, 15, 2433–2463, https://doi.org/10.5194/amt-15-2433-2022, 2022.

Babenhauserheide, A., Hase, F., and Morino, I.: Net CO_2 fossil fuel emissions of Tokyo estimated directly from measurements of the Tsukuba TCCON site and radiosondes, Atmospheric Measurement Techniques, 13, 2697–2710, https://doi.org/10.5194/amt-13-2697-2020, 2020.

Beirle, S., Borger, C., Dörner, S., Li, A., Hu, Z., Liu, F., Wang, Y., and Wagner, T.: Pinpointing nitrogen oxide emissions from space, Science Advances, 5, eaax9800, https://doi.org/10.1126/sciadv.aax9800, 2019.

Beirle, S., Borger, C., Dörner, S., Eskes, H., Kumar, V., De Laat, A., and Wagner, T.: Catalog of NO_x emissions from point sources as derived from the divergence of the NO_2 flux for TROPOMI, Earth System Science Data, 13, 2995–3012, https://doi.org/10.5194/essd-13-2995-2021, 2021.

Brenny, B., Day, J., de Goeij, B., Palombo, E., Ouwerkerk, B., Koc, N. A., Bell, A., Leemhuis, A., Paskeviciute, A., Buisset, C., and Malavart, A.: Development of spectrometers for the TANGO greenhouse gas monitoring missions, in: International Conference on Space Optics — ICSO 2022, edited by Minoglou, K., Karafolas, N., and Cugny, B., vol. 12777, p. 127771S, International Society for Optics and Photonics, SPIE, https://doi.org/10.1117/12.2689936, 2023.

Brown, D., Sadiq, R., and Hewage, K.: An overview of air emission intensities and environmental performance of grey cement manufacturing in Canada, Clean Technologies and Environmental Policy, 16, 1119–1131, https://doi.org/10.1007/s10098-014-0714-y, 2014.

Butz, A., Guerlet, S., Hasekamp, O., Schepers, D., Galli, A., Aben, I., Frankenberg, C., Hartmann, J.-M., Tran, H., Kuze, A., Keppel-Aleks, G., Toon, G., Wunch, D., Wennberg, P., Deutscher, N., Griffith, D., Macatangay, R., Messerschmidt, J., Notholt, J., and Warneke, T.: Toward accurate CO_2 and CH_4 observations from GOSAT, Geophysical Research Letters, 38, https://doi.org/10.1029/2011GL047888, 2011.

Butz, A., Dinger, A. S., Bobrowski, N., Kostinek, J., Fieber, L., Fischerkeller, C., Giuffrida, G. B., Hase, F., Klappenbach, F., Kuhn, J., Lübcke, P., Tirpitz, L., and Tu, Q.: Remote sensing of volcanic CO_2, HF, HCl, SO_2, and BrO in the downwind plume of Mt. Etna, Atmospheric Measurement Techniques, 10, 1–14, https://doi.org/10.5194/amt-10-1-2017, 2017.

Butz, A., Hanft, V., Kleinschek, R., Frey, M. M., Müller, A., Knapp, M., Morino, I., Agusti-Panareda, A., Hase, F., Landgraf, J., Vardag, S., and Tanimoto, H.: Versatile and Targeted Validation of Space-Borne XCO_2, XCH_4 and XCO Observations by Mobile Ground-Based Direct-Sun Spectrometers, Frontiers in Remote Sensing, 2, 775 805, https://doi.org/10.3389/frsen.2021.775805, 2022.

Bösch, H., Camy-Peyret, C., Chipperfield, M. P., Fitzenberger, R., Harder, H., Platt, U., and Pfeilsticker, K.: Upper limits of stratospheric IO and OIO inferred from center-to-limb-darkening-corrected balloon-borne solar occultation visible spectra: Implications for total gaseous iodine and stratospheric ozone, Journal of Geophysical Research: Atmospheres, 108, 2002JD003 078, https://doi.org/10.1029/2002JD003078, 2003.

Cede, A., Herman, J., Richter, A., Krotkov, N., and Burrows, J.: Measurements of nitrogen dioxide total column amounts using
540   a Brewer double spectrophotometer in direct Sun mode, Journal of Geophysical Research: Atmospheres, 111, 2005JD006 585,
https://doi.org/10.1029/2005JD006585, 2006.

Chance, K. and Kurucz, R.: An improved high-resolution solar reference spectrum for earth's atmosphere measurements in
the ultraviolet, visible, and near infrared, Journal of Quantitative Spectroscopy and Radiative Transfer, 111, 1289–1295,
https://doi.org/10.1016/j.jqsrt.2010.01.036, 2010.

545   Charuvil Asokan, H., Landgraf, J., Veefkind, P., Dellaert, S., and Butz, A.: Assessing the Detection Potential of Targeting Satellites for Global
Greenhouse Gas Monitoring: Insights from TANGO Simulations, EGUsphere, 2025, 1–27, https://doi.org/10.5194/egusphere-2025-1071,
2025.

Chen, T.-M., Kuschner, W. G., Gokhale, J., and Shofer, S.: Outdoor Air Pollution: Nitrogen Dioxide, Sulfur Dioxide, and Carbon Monoxide
Health Effects, The American Journal of the Medical Sciences, 333, 249–256, https://doi.org/10.1097/MAJ.0b013e31803b900f, 2007.

550   Climate TRACE coalition: Climate TRACE - Tracking Realtime Atmospheric Carbon Emissions: Climate TRACE Emissions Inventory,
https://climatetrace.org, accessed: 20.02.2024., 2022.

Crippa, M., Guizzardi, D., Muntean, M., Schaaf, E., Dentener, F., Van Aardenne, J. A., Monni, S., Doering, U., Olivier, J. G. J., Pagliari, V.,
and Janssens-Maenhout, G.: Gridded emissions of air pollutants for the period 1970–2012 within EDGAR v4.3.2, Earth System Science
Data, 10, 1987–2013, https://doi.org/10.5194/essd-10-1987-2018, 2018.

555   Crippa, M., Guizzardi, D., Pagani, F., Schiavina, M., Melchiorri, M., Pisoni, E., Graziosi, F., Muntean, M., Maes, J., Dijkstra, L., Van Damme,
M., Clarisse, L., and Coheur, P.: Insights on the spatial distribution of global, national and sub-national GHG emissions in EDGARv8.0,
Earth System Science Data, 16, 2811–2830, https://doi.org/10.5194/essd-16-2811-2024, 2024.

Czerny, M. and Turner, A.: Über den Astigmatismus bei Spiegelspektrometern, Zeitschrift für Physik, 61, 792–797, 1930.

Danckaert, T., Fayt, C., Van Roozendael, M., De Smedt, I., Letocart, V., Merlaud, A., and Pinardi, G.: QDOAS. Software user manual.
560   Version 3.2., Royal Belgian Institute for Space Aeronomy, 2017.

Dentener, F., van Weele, M., Krol, M., Houweling, S., and van Velthoven, P.: Trends and inter-annual variability of methane emissions
derived from 1979–1993 global CTM simulations, Atmos. Chem. Phys., 3, 73–88, 2003.

Dietrich, F., Chen, J., Voggenreiter, B., Aigner, P., Nachtigall, N., and Reger, B.: MUCCnet: Munich Urban Carbon Column network, 14,
1111–1126, https://doi.org/10.5194/amt-14-1111-2021, 2021.

565   Eldering, A., Wennberg, P. O., Crisp, D., Schimel, D. S., Gunson, M. R., Chatterjee, A., Liu, J., Schwandner, F. M., Sun, Y.,
O'Dell, C. W., Frankenberg, C., Taylor, T., Fisher, B., Osterman, G. B., Wunch, D., Hakkarainen, J., Tamminen, J., and Weir,
B.: The Orbiting Carbon Observatory-2 early science investigations of regional carbon dioxide fluxes, Science, 358, eaam5745,
https://doi.org/10.1126/science.aam5745, 2017.

Fontaras, G., Franco, V., Dilara, P., Martini, G., and Manfredi, U.: Development and review of Euro 5 passenger car emis-
570   sion factors based on experimental results over various driving cycles, Science of The Total Environment, 468-469, 1034–1042,
https://doi.org/10.1016/j.scitotenv.2013.09.043, 2014.

Frey, M., Hase, F., Blumenstock, T., Groß, J., Kiel, M., Mengistu Tsidu, G., Schäfer, K., Sha, M. K., and Orphal, J.: Calibration and
instrumental line shape characterization of a set of portable FTIR spectrometers for detecting greenhouse gas emissions, Atmospheric
Measurement Techniques, 8, 3047–3057, https://doi.org/10.5194/amt-8-3047-2015, 2015.

575   Frey, M., Sha, M. K., Hase, F., Kiel, M., Blumenstock, T., Harig, R., Surawicz, G., Deutscher, N. M., Shiomi, K., Franklin, J. E., Bösch, H.,
Chen, J., Grutter, M., Ohyama, H., Sun, Y., Butz, A., Tsidu, G. M., Ene, D., Wunch, D., Cao, Z., Garcia, O., Ramonet, M., Vogel, F., and

Orphal, J.: Building the COllaborative Carbon Column Observing Network (COCCON): long-term stability and ensemble performance of the EM27/SUN Fourier transform spectrometer, Atmospheric Measurement Techniques, 12, 1513–1530, https://doi.org/10.5194/amt-12-1513-2019, 2019.

580 Frey, M. M., Hase, F., Blumenstock, T., Dubravica, D., Groß, J., Göttsche, F., Handjaba, M., Amadhila, P., Mushi, R., Morino, I., Shiomi, K., Sha, M. K., De Mazière, M., and Pollard, D. F.: Long-term column-averaged greenhouse gas observations using a COCCON spectrometer at the high-surface-albedo site in Gobabeb, Namibia, Atmospheric Measurement Techniques, 14, 5887–5911, https://doi.org/10.5194/amt-14-5887-2021, 2021.

Gisi, M., Hase, F., Dohe, S., Blumenstock, T., Simon, A., and Keens, A.: XCO_2-measurements with a tabletop FTS using solar absorption
585 spectroscopy, Atmospheric Measurement Techniques, 5, 2969–2980, https://doi.org/10.5194/amt-5-2969-2012, 2012.

Gordon, I., Rothman, L., Hill, C., Kochanov, R., Tan, Y., Bernath, P., Birk, M., Boudon, V., Campargue, A., Chance, K., Drouin, B., Flaud, J.-M., Gamache, R., Hodges, J., Jacquemart, D., Perevalov, V., Perrin, A., Shine, K., Smith, M.-A., Tennyson, J., Toon, G., Tran, H., Tyuterev, V., Barbe, A., Császár, A., Devi, V., Furtenbacher, T., Harrison, J., Hartmann, J.-M., Jolly, A., Johnson, T., Karman, T., Kleiner, I., Kyuberis, A., Loos, J., Lyulin, O., Massie, S., Mikhailenko, S., Moazzen-Ahmadi, N., Müller, H., Naumenko, O., Nikitin, A., Polyansky,
590 O., Rey, M., Rotger, M., Sharpe, S., Sung, K., Starikova, E., Tashkun, S., Auwera, J. V., Wagner, G., Wilzewski, J., Wcisło, P., Yu, S., and Zak, E.: The HITRAN2016 molecular spectroscopic database, Journal of Quantitative Spectroscopy and Radiative Transfer, 203, 3–69, https://doi.org/10.1016/j.jqsrt.2017.06.038, 2017.

Grossmann, K., Frankenberg, C., Magney, T. S., Hurlock, S. C., Seibt, U., and Stutz, J.: PhotoSpec: A new instrument to measure spatially distributed red and far-red Solar-Induced Chlorophyll Fluorescence, Remote Sensing of Environment, 216, 311–327,
595 https://doi.org/10.1016/j.rse.2018.07.002, 2018.

Guevara, M., Enciso, S., Tena, C., Jorba, O., Dellaert, S., Denier Van Der Gon, H., and Pérez García-Pando, C.: A global catalogue of CO_2 emissions and co-emitted species from power plants at a very high spatial and temporal resolution, Earth System Science Data, 16, 337–373, https://doi.org/10.5194/essd-2023-95, 2024.

Hanft, V.: Application and Refinement of a Mobile Remote Sensing Setup on Board of a Research Vessel in the Western North Pacific,
600 Master thesis, Heidelberg University, 2021.

Hase, F.: Inversion von Spurengasprofilen aus hochaufgelösten bodengebundenen FTIR-Messungen in Absorption, PhD Thesis, Forschungszentrum Karlsruhe, Karlsruhe, 2000.

Hase, F., Frey, M., Kiel, M., Blumenstock, T., Harig, R., Keens, A., and Orphal, J.: Addition of a channel for XCO observations to a portable FTIR spectrometer for greenhouse gas measurements, Atmospheric Measurement Techniques, 9, 2303–2313, https://doi.org/10.5194/amt-
605 9-2303-2016, 2016.

Herkommer, B., Alberti, C., Castracane, P., Chen, J., Dehn, A., Dietrich, F., Deutscher, N. M., Frey, M. M., Groß, J., Gillespie, L., Hase, F., Morino, I., Pak, N. M., Walker, B., and Wunch, D.: Using a portable FTIR spectrometer to evaluate the consistency of Total Carbon Column Observing Network (TCCON) measurements on a global scale: the Collaborative Carbon Column Observing Network (COCCON) travel standard, Atmospheric Measurement Techniques, 17, 3467–3494, https://doi.org/10.5194/amt-17-3467-2024, 2024.

610 Herman, J., Cede, A., Spinei, E., Mount, G., Tzortziou, M., and Abuhassan, N.: NO_2 column amounts from ground-based Pandora and MF-DOAS spectrometers using the direct-sun DOAS technique: Intercomparisons and application to OMI validation, Journal of Geophysical Research: Atmospheres, 114, D13 307, https://doi.org/10.1029/2009JD011848, 2009.

Hersbach, H., Bell, B., Berrisford, P., Hirahara, S., Horányi, A., Muñoz-Sabater, J., Nicolas, J., Peubey, C., Radu, R., Schepers, D., Simmons, A., Soci, C., Abdalla, S., Abellan, X., Balsamo, G., Bechtold, P., Biavati, G., Bidlot, J., Bonavita, M., De Chiara, G., Dahlgren, P., Dee,

615   D., Diamantakis, M., Dragani, R., Flemming, J., Forbes, R., Fuentes, M., Geer, A., Haimberger, L., Healy, S., Hogan, R. J., Hólm, E., Janisková, M., Keeley, S., Laloyaux, P., Lopez, P., Lupu, C., Radnoti, G., De Rosnay, P., Rozum, I., Vamborg, F., Villaume, S., and Thépaut, J.: The ERA5 global reanalysis, Quarterly Journal of the Royal Meteorological Society, 146, 1999–2049, https://doi.org/10.1002/qj.3803, 2020.

Hu, H., Hasekamp, O., Butz, A., Galli, A., Landgraf, J., Aan de Brugh, J., Borsdorff, T., Scheepmaker, R., and Aben, I.: The operational
620   methane retrieval algorithm for TROPOMI, Atmospheric Measurement Techniques, 9, 5423–5440, https://doi.org/10.5194/amt-9-5423-2016, 2016.

Huijnen, V., Williams, J., van Weele, M., van Noije, T., Krol, M., Dentener, F., Segers, A., Houweling, S., Peters, W., de Laat, J., Boersma, F., Bergamaschi, P., van Velthoven, P., Le Sager, P., Eskes, H., Alkemade, F., Scheele, R., Nédélec, P., and Pätz, H.-W.: The global chemistry transport model TM5: description and evaluation of the tropospheric chemistry version 3.0, Geoscientific Model Development,
625   3, 445–473, https://doi.org/10.5194/gmd-3-445-2010, 2010.

Humpage, N., Boesch, H., Okello, W., Dietrich, F., Chen, J., Lunt, M., Feng, L., Palmer, P., and Hase, F.: Greenhouse gas column observations from a portable spectrometer in Uganda, EGU General Assembly 2021, online, 19–30 Apr 2021, EGU21-10156, https://doi.org/10.5194/egusphere-egu21-10156, 2021.

IEA-AMF: Advanced Motor Fuels in Japan, https://iea-amf.org/content/publications/country_reports/japan#_ftn9, accessed: 01.07.2025,
630   2023.

Imasu, R., Matsunaga, T., Nakajima, M., Yoshida, Y., Shiomi, K., Morino, I., Saitoh, N., Niwa, Y., Someya, Y., Oishi, Y., Hashimoto, M., Noda, H., Hikosaka, K., Uchino, O., Maksyutov, S., Takagi, H., Ishida, H., Nakajima, T. Y., Nakajima, T., and Shi, C.: Greenhouse gases Observing SATellite 2 (GOSAT-2): mission overview, Progress in Earth and Planetary Science, 10, 33, https://doi.org/10.1186/s40645-023-00562-2, 2023.

635   Janssens-Maenhout, G., Crippa, M., Guizzardi, D., Muntean, M., Schaaf, E., Dentener, F., Bergamaschi, P., Pagliari, V., Olivier, J. G. J., Peters, J. A. H. W., Van Aardenne, J. A., Monni, S., Doering, U., Petrescu, A. M. R., Solazzo, E., and Oreggioni, G. D.: EDGAR v4.3.2 Global Atlas of the three major greenhouse gas emissions for the period 1970–2012, Earth System Science Data, 11, 959–1002, https://doi.org/10.5194/essd-11-959-2019, 2019.

Japan Electric Power Exchange: Outtage information list, https://hjks.jepx.or.jp/hjks/outages, accessed: 28.10.2024, 2024.
640   Jera Corporation: Power station list, https://www.jera.co.jp/en/corporate/business/thermal-power/list, accessed: 02.07.2025, 2025.

Jones, T. S., Franklin, J. E., Chen, J., Dietrich, F., Hajny, K. D., Paetzold, J. C., Wenzel, A., Gately, C., Gottlieb, E., Parker, H., Dubey, M., Hase, F., Shepson, P. B., Mielke, L. H., and Wofsy, S. C.: Assessing urban methane emissions using column-observing portable Fourier transform infrared (FTIR) spectrometers and a novel Bayesian inversion framework, Atmospheric Chemistry and Physics, 21, 13 131–13 147, https://doi.org/10.5194/acp-21-13131-2021, 2021.

645   Kesgin, U. and Vardar, N.: A study on exhaust gas emissions from ships in Turkish Straits, Atmospheric Environment, 35, 1863–1870, https://doi.org/10.1016/S1352-2310(00)00487-8, 2001.

Kiel, M., Eldering, A., Roten, D. D., Lin, J. C., Feng, S., Lei, R., Lauvaux, T., Oda, T., Roehl, C. M., Blavier, J.-F., and Iraci, L. T.: Urban-focused satellite CO_2 observations from the Orbiting Carbon Observatory-3: A first look at the Los Angeles megacity, Remote Sensing of Environment, 258, 112 314, https://doi.org/10.1016/j.rse.2021.112314, 2021.

650   Klappenbach, F., Bertleff, M., Kostinek, J., Hase, F., Blumenstock, T., Agusti-Panareda, A., Razinger, M., and Butz, A.: Accurate mobile remote sensing of XCO_2 and XCH_4 latitudinal transects from aboard a research vessel, Atmospheric Measurement Techniques, 8, 5023–5038, https://doi.org/10.5194/amt-8-5023-2015, 2015.

Klemm, W. and Hoppe, R.: Anorganische Chemie, Sammlung Göschen, de Gruyter, Berlin, New York, 1980.

Knapp, M., Kleinschek, R., Hase, F., Agustí-Panareda, A., Inness, A., Barré, J., Landgraf, J., Borsdorff, T., Kinne, S., and Butz, A.: Shipborne
655   measurements of XCO_2, XCH_4, and XCO above the Pacific Ocean and comparison to CAMS atmospheric analyses and S5P/TROPOMI,
Earth System Science Data, 13, 199–211, https://doi.org/10.5194/essd-13-199-2021, 2021.

Krautwurst, S., Gerilowski, K., Jonsson, H. H., Thompson, D. R., Kolyer, R. W., Iraci, L. T., Thorpe, A. K., Horstjann, M., Eastwood, M.,
Leifer, I., Vigil, S. A., Krings, T., Borchardt, J., Buchwitz, M., Fladeland, M. M., Burrows, J. P., and Bovensmann, H.: Methane emissions
from a Californian landfill, determined from airborne remote sensing and in situ measurements, Atmospheric Measurement Techniques,
660   10, 3429–3452, https://doi.org/10.5194/amt-10-3429-2017, 2017.

Kuhlmann, G., Henne, S., Meijer, Y., and Brunner, D.: Quantifying CO_2 Emissions of Power Plants With CO_2 and NO_2 Imaging Satellites,
Frontiers in Remote Sensing, 2, 689 838, https://doi.org/10.3389/frsen.2021.689838, 2021.

Kurokawa, J. and Ohara, T.: Long-term historical trends in air pollutant emissions in Asia: Regional Emission inventory in ASia (REAS)
version 3, Atmospheric Chemistry and Physics, 20, 12 761–12 793, https://doi.org/10.5194/acp-20-12761-2020, 2020.

665 Landgraf, J., aan de Brugh, J., Scheepmaker, R., Borsdorff, T., Hu, H., Houweling, S., Butz, A., Aben, I., and Hasekamp, O.: Carbon
monoxide total column retrievals from TROPOMI shortwave infrared measurements, Atmospheric Measurement Techniques, 9, 4955–
4975, https://doi.org/10.5194/amt-9-4955-2016, 2016.

Langley, S. P.: On a Possible Variation of the Solar Radiation and its Probable Effect on Terrestrial Temperatures, The Astrophysical Journal,
19, 305–321, https://doi.org/10.1086/141120, 1904.

670 Laughner, J. L., Toon, G. C., Mendonca, J., Petri, C., Roche, S., Wunch, D., Blavier, J.-F., Griffith, D. W. T., Heikkinen, P., Keeling, R. F.,
Kiel, M., Kivi, R., Roehl, C. M., Stephens, B. B., Baier, B. C., Chen, H., Choi, Y., Deutscher, N. M., DiGangi, J. P., Gross, J., Herkommer,
B., Jeseck, P., Laemmel, T., Lan, X., McGee, E., McKain, K., Miller, J., Morino, I., Notholt, J., Ohyama, H., Pollard, D. F., Rettinger,
M., Riris, H., Rousogenous, C., Sha, M. K., Shiomi, K., Strong, K., Sussmann, R., Té, Y., Velazco, V. A., Wofsy, S. C., Zhou, M., and
Wennberg, P. O.: The Total Carbon Column Observing Network's GGG2020 data version, Earth System Science Data, 16, 2197–2260,
675   https://doi.org/10.5194/essd-16-2197-2024, 2024.

Leifer, I., Melton, C., Fischer, M. L., Fladeland, M., Frash, J., Gore, W., Iraci, L. T., Marrero, J. E., Ryoo, J.-M., Tanaka, T., and Yates,
E. L.: Atmospheric characterization through fused mobile airborne and surface in situ surveys: methane emissions quantification from a
producing oil field, Atmospheric Measurement Techniques, 11, 1689–1705, https://doi.org/10.5194/amt-11-1689-2018, 2018.

Liu, J., Tong, D., Zheng, Y., Cheng, J., Qin, X., Shi, Q., Yan, L., Lei, Y., and Zhang, Q.: Carbon and air pollutant emissions from
680   China's cement industry 1990–2015: trends, evolution of technologies, and drivers, Atmospheric Chemistry and Physics, 21, 1627–1647,
https://doi.org/10.5194/acp-21-1627-2021, 2021.

Luther, A., Kleinschek, R., Scheidweiler, L., Defratyka, S., Stanisavljevic, M., Forstmaier, A., Dandocsi, A., Wolff, S., Dubravica, D.,
Wildmann, N., Kostinek, J., Jöckel, P., Nickl, A.-L., Klausner, T., Hase, F., Frey, M., Chen, J., Dietrich, F., Necki, J., Swolkien, J., Fix,
A., Roiger, A., and Butz, A.: Quantifying CH_4 emissions from hard coal mines using mobile sun-viewing Fourier transform spectrometry,
685   Atmospheric Measurement Techniques, 12, 5217–5230, https://doi.org/10.5194/amt-12-5217-2019, 2019.

Luther, A., Kostinek, J., Kleinschek, R., Defratyka, S., Stanisavljević, M., Forstmaier, A., Dandocsi, A., Scheidweiler, L., Dubravica, D.,
Wildmann, N., Hase, F., Frey, M. M., Chen, J., Dietrich, F., Necki, J., Swolkień, J., Knote, C., Vardag, S. N., Roiger, A., and Butz,
A.: Observational constraints on methane emissions from Polish coal mines using a ground-based remote sensing network, Atmospheric
Chemistry and Physics, 22, 5859–5876, https://doi.org/10.5194/acp-22-5859-2022, 2022.

690 Löw, B. A., Kleinschek, R., Enders, V., Sander, S. P., Pongetti, T. J., Schmitt, T. D., Hase, F., Kostinek, J., and Butz, A.: A portable reflected-sunlight spectrometer for CO_2 and CH_4, Atmospheric Measurement Techniques, 16, 5125–5144, https://doi.org/10.5194/amt-16-5125-2023, 2023.

Manisalidis, I., Stavropoulou, E., Stavropoulos, A., and Bezirtzoglou, E.: Environmental and Health Impacts of Air Pollution: A Review, Frontiers in Public Health, 8, 14, https://doi.org/10.3389/fpubh.2020.00014, 2020.

695 Meirink, J. F., Eskes, H. J., and Goede, A. P. H.: Sensitivity analysis of methane emissions derived from SCIAMACHY observations through inverse modelling, Atmos. Chem. Phys., 6, 1275–1292, https://doi.org/10.5194/acp-6-1275-2006, 2006.

Mertz, L.: Auxiliary computation for Fourier transform spectrometry, Infrared Physics, 7, 17–23, 1967.

Müller, A., Tanimoto, H., Sugita, T., Machida, T., Nakaoka, S.-i., Patra, P. K., Laughner, J., and Crisp, D.: New approach to evaluate satellite-derived XCO_2 over oceans by integrating ship and aircraft observations, Atmospheric Chemistry and Physics, 21, 8255–8271,
700 https://doi.org/10.5194/acp-21-8255-2021, 2021.

National Centers for Environmental Prediction, National Weather Service, NOAA, and U.S. Department of Commerce: NCEP FNL Operational Model Global Tropospheric Analyses, continuing from July 1999, https://doi.org/10.5065/D6M043C6, research Data Archive at the National Center for Atmospheric Research, Computational and Information Systems Laboratory, Boulder, Colo. (Updated daily). Last accessed: 19.05.2024., 2000.

705 Neckel, H.: Spectral Atlas of Solar Absolute Disk-averaged and Disk-center Intensity from 3290 to 12510 A, 1987.

Nippon Kaiji Kyokai: Registry of ships: Nichiyu Maru, https://www.classnk.or.jp/register/regships/one_dsp.aspx?imo=9846201, accessed: 25.04.2024., 2024.

Nippon Steel Corporation: Fact Book 2023, https://www.nipponsteel.com/en/factbook/2023/, accessed: 23.04.2024., 2024.

Norton, R. H. and Beer, R.: New apodizing functions for Fourier spectrometry, Journal of the Optical Society of America, 66, 259–264,
710 https://doi.org/10.1364/JOSA.66.000259, 1976.

Norton, R. H. and Beer, R.: Errata: New apodizing functions for Fourier spectrometry, Journal of the Optical Society of America, 67, 419–419, https://doi.org/10.1364/JOSA.67.000419, 1977.

Ocean Optics, Inc.: QE Pro Scientific-grade Spectrometer, Installation and Operation Manual, 2014.

Ohyama, H., Morino, I., Nagahama, T., Machida, T., Suto, H., Oguma, H., Sawa, Y., Matsueda, H., Sugimoto, N., Nakane, H., and Nakagawa,
715 K.: Column-averaged volume mixing ratio of CO_2 measured with ground-based Fourier transform spectrometer at Tsukuba, Journal of Geophysical Research: Atmospheres, 114, D18 303, https://doi.org/10.1029/2008JD011465, 2009.

Ohyama, H., Frey, M. M., Morino, I., Shiomi, K., Nishihashi, M., Miyauchi, T., Yamada, H., Saito, M., Wakasa, M., Blumenstock, T., and Hase, F.: Anthropogenic CO_2 emission estimates in the Tokyo metropolitan area from ground-based CO_2 column observations, 23, 15 097–15 119, https://doi.org/10.5194/acp-23-15097-2023, 2023.

720 O'Shea, S. J., Allen, G., Fleming, Z. L., Bauguitte, S. J., Percival, C. J., Gallagher, M. W., Lee, J., Helfter, C., and Nemitz, E.: Area fluxes of carbon dioxide, methane, and carbon monoxide derived from airborne measurements around Greater London: A case study during summer 2012, Journal of Geophysical Research: Atmospheres, 119, 4940–4952, https://doi.org/10.1002/2013JD021269, 2014.

Park, H., Jeong, S., Park, H., Labzovskii, L. D., and Bowman, K. W.: An assessment of emission characteristics of Northern Hemisphere cities using spaceborne observations of CO_2, CO, and NO_2, Remote Sensing of Environment, 254, 112 246,
725 https://doi.org/10.1016/j.rse.2020.112246, 2021.

Peters, W., Jacobson, A. R., Sweeney, C., Andrews, A. E., Conway, T. J., Masarie, K., Miller, J. B., Bruhwiler, L. M. P., Petron, G., Hirsch, A. I., Worthy, D. E. J., van der Werf, G. R., Randerson, J. T., Wennberg, P. O., Krol, M. C., and Tans, P. P.: An atmospheric perspective

on North American carbon dioxide exchange: CarbonTracker, Proceedings of the National Academy of Sciences, 104, 18 925–18 930, https://doi.org/10.1073/pnas.0708986104, 2007.

730 Phillips, D. L.: A Technique for the Numerical Solution of Certain Integral Equations of the First Kind, Journal of the ACM, 9, 84–97, https://doi.org/10.1145/321105.321114, 1962.

Piters, A. J. M., Boersma, K. F., Kroon, M., Hains, J. C., Van Roozendael, M., Wittrock, F., Abuhassan, N., Adams, C., Akrami, M., Allaart, M. A. F., Apituley, A., Beirle, S., Bergwerff, J. B., Berkhout, A. J. C., Brunner, D., Cede, A., Chong, J., Clémer, K., Fayt, C., Frieß, U., Gast, L. F. L., Gil-Ojeda, M., Goutail, F., Graves, R., Griesfeller, A., Großmann, K., Hemerijckx, G., Hendrick, F., Henzing,
735 B., Herman, J., Hermans, C., Hoexum, M., Van Der Hoff, G. R., Irie, H., Johnston, P. V., Kanaya, Y., Kim, Y. J., Klein Baltink, H., Kreher, K., De Leeuw, G., Leigh, R., Merlaud, A., Moerman, M. M., Monks, P. S., Mount, G. H., Navarro-Comas, M., Oetjen, H., Pazmino, A., Perez-Camacho, M., Peters, E., Du Piesanie, A., Pinardi, G., Puentedura, O., Richter, A., Roscoe, H. K., Schönhardt, A., Schwarzenbach, B., Shaiganfar, R., Sluis, W., Spinei, E., Stolk, A. P., Strong, K., Swart, D. P. J., Takashima, H., Vlemmix, T., Vrekoussis, M., Wagner, T., Whyte, C., Wilson, K. M., Yela, M., Yilmaz, S., Zieger, P., and Zhou, Y.: The Cabauw Intercomparison campaign for
740 Nitrogen Dioxide measuring Instruments (CINDI): design, execution, and early results, Atmospheric Measurement Techniques, 5, 457–485, https://doi.org/10.5194/amt-5-457-2012, 2012.

Platt, U. and Stutz, J.: Differential optical absorption spectroscopy, Physics of earth and space environments, Springer, Berlin, Heidelberg, 2008.

Reuter, M., Buchwitz, M., Hilboll, A., Richter, A., Schneising, O., Hilker, M., Heymann, J., Bovensmann, H., and Burrows, J. P.:
745 Decreasing emissions of NO_x relative to CO_2 in East Asia inferred from satellite observations, Nature Geoscience, 7, 792–795, https://doi.org/10.1038/ngeo2257, 2014.

Rothman, L., Gordon, I., Barbe, A., Benner, D., Bernath, P., Birk, M., Boudon, V., Brown, L., Campargue, A., Champion, J.-P., Chance, K., Coudert, L., Dana, V., Devi, V., Fally, S., Flaud, J.-M., Gamache, R., Goldman, A., Jacquemart, D., Kleiner, I., Lacome, N., Lafferty, W., Mandin, J.-Y., Massie, S., Mikhailenko, S., Miller, C., Moazzen-Ahmadi, N., Naumenko, O., Nikitin, A., Orphal, J., Perevalov, V., Perrin,
750 A., Predoi-Cross, A., Rinsland, C., Rotger, M., Šimečková, M., Smith, M., Sung, K., Tashkun, S., Tennyson, J., Toth, R., Vandaele, A., and Vander Auwera, J.: The HITRAN 2008 molecular spectroscopic database, Journal of Quantitative Spectroscopy and Radiative Transfer, 110, 533–572, https://doi.org/10.1016/j.jqsrt.2009.02.013, 2009.

Schneising, O., Buchwitz, M., Reuter, M., Weimer, M., Bovensmann, H., Burrows, J. P., and Bösch, H.: Towards a sector-specific CO/CO_2 emission ratio: Satellite-based observation of CO release from steel production in Germany, Atmospheric Chemistry and Physics, 24,
755 7609–7621, https://doi.org/10.5194/acp-24-7609-2024, 2024.

Serdyuchenko, A., Gorshelev, V., Weber, M., Chehade, W., and Burrows, J. P.: High spectral resolution ozone absorption cross-sections – Part 2: Temperature dependence, Atmospheric Measurement Techniques, 7, 625–636, https://doi.org/10.5194/amt-7-625-2014, 2014.

Sierk, B., Fernandez, V., Bézy, J.-L., Meijer, Y., Durand, Y., Courrèges-Lacoste, G. B., Pachot, C., Löscher, A., Nett, H., Minoglou, K., Boucher, L., Windpassinger, R., Pasquet, A., Serre, D., and te Hennepe, F.: The Copernicus CO2M mission for monitoring anthropogenic
760 carbon dioxide emissions from space, in: International Conference on Space Optics — ICSO 2020, edited by Cugny, B., Sodnik, Z., and Karafolas, N., vol. 11852, p. 118523M, International Society for Optics and Photonics, SPIE, https://doi.org/10.1117/12.2599613, 2021.

Spietz, P.: Absorption Cross Sections for Iodine Species of Relevance to the Photolysis of Mixtures of I_2 and O_3 and for the Atmosphere, PhD thesis, University of Bremen, 2005.

Srivastava, R., Neuffer, W., Grano, D., Khan, S., Staudt, J., and Jozewicz, W.: Controlling NO_x emission from industrial sources, Environ-
765 mental Progress, 24, 181–197, https://doi.org/10.1002/ep.10063, 2005.

Statistics Bureau of Japan: Population and households of Japan 2020, https://www.stat.go.jp/english/data/kokusei/2020/summary/pdf/all.pdf, accessed: 01.07.2025, 2020.

Stutz, J., Werner, B., Spolaor, M., Scalone, L., Festa, J., Tsai, C., Cheung, R., Colosimo, S. F., Tricoli, U., Raecke, R., Hossaini, R., Chipperfield, M. P., Feng, W., Gao, R.-S., Hintsa, E. J., Elkins, J. W., Moore, F. L., Daube, B., Pittman, J., Wofsy, S., and Pfeilsticker, K.:
770   A new Differential Optical Absorption Spectroscopy instrument to study atmospheric chemistry from a high-altitude unmanned aircraft, Atmospheric Measurement Techniques, 10, 1017–1042, https://doi.org/10.5194/amt-10-1017-2017, 2017.

Tanimoto, H., Matsunaga, T., Someya, Y., Fujinawa, T., Ohyama, H., Morino, I., Yashiro, H., Sugita, T., Inomata, S., Müller, A., Saeki, T., Yoshida, Y., Niwa, Y., Saito, M., Noda, H., Yamashita, Y., Ikeda, K., Saigusa, N., Machida, T., Frey, M. M., Lim, H., Srivastava, P., Jin, Y., Shimizu, A., Nishizawa, T., Kanaya, Y., Sekiya, T., Patra, P., Takigawa, M., Bisht, J., Kasai, Y., and Sato, T. O.: The greenhouse
775   gas observation mission with Global Observing SATellite for Greenhouse gases and Water cycle (GOSAT-GW): objectives, conceptual framework and scientific contributions, Progress in Earth and Planetary Science, 12, 8, https://doi.org/10.1186/s40645-025-00684-9, 2025.

Taylor, T. E., Eldering, A., Merrelli, A., Kiel, M., Somkuti, P., Cheng, C., Rosenberg, R., Fisher, B., Crisp, D., Basilio, R., Bennett, M., Cervantes, D., Chang, A., Dang, L., Frankenberg, C., Haemmerle, V. R., Keller, G. R., Kurosu, T., Laughner, J. L., Lee, R., Marchetti, Y., Nelson, R. R., O'Dell, C. W., Osterman, G., Pavlick, R., Roehl, C., Schneider, R., Spiers, G., To, C., Wells, C., Wennberg, P. O., Yela-
780   manchili, A., and Yu, S.: OCO-3 early mission operations and initial (vEarly) XCO$_2$ and SIF retrievals, Remote Sensing of Environment, 251, 112 032, https://doi.org/10.1016/j.rse.2020.112032, 2020.

Thalman, R. and Volkamer, R.: Temperature dependent absorption cross-sections of O$_2$–O$_2$ collision pairs between 340 and 630 nm and at atmospherically relevant pressure, Physical Chemistry Chemical Physics, 15, 15 371–15 381, https://doi.org/10.1039/c3cp50968k, 2013.

Tikhonov, A. N.: O reschenii nekorrektno postawlennüch sadatsch i metode regularisazii, Dokladü Akademii Nauk SSSR, 151, 501–504,
785   1963.

Van der Maas, L.: Evaluating blast furnace emissions using high resolution TROPOMI CO and NO$_x$ measurements and emission inventory data, Master thesis, Wageningen University and Research, 2019.

Van Geffen, J., Eskes, H., Compernolle, S., Pinardi, G., Verhoelst, T., Lambert, J.-C., Sneep, M., Ter Linden, M., Ludewig, A., Boersma, K. F., and Veefkind, J. P.: Sentinel-5P TROPOMI NO$_2$ retrieval: impact of version v2.2 improvements and comparisons with OMI and
790   ground-based data, Atmospheric Measurement Techniques, 15, 2037–2060, https://doi.org/10.5194/amt-15-2037-2022, 2022.

Vandaele, A., Hermans, C., Simon, P., Carleer, M., Colin, R., Fally, S., Mérienne, M., Jenouvrier, A., and Coquart, B.: Measurements of the NO$_2$ absorption cross-section from 42 000 cm-1 to 10 000 cm-1 (238-1000 nm) at 220 K and 294 K, Journal of Quantitative Spectroscopy and Radiative Transfer, 59, 171–184, https://doi.org/10.1016/S0022-4073(97)00168-4, 1998.

Viatte, C., Lauvaux, T., Hedelius, J. K., Parker, H., Chen, J., Jones, T., Franklin, J. E., Deng, A. J., Gaudet, B., Verhulst, K., Duren, R., Wunch,
795   D., Roehl, C., Dubey, M. K., Wofsy, S., and Wennberg, P. O.: Methane emissions from dairies in the Los Angeles Basin, Atmospheric Chemistry and Physics, 17, 7509–7528, https://doi.org/10.5194/acp-17-7509-2017, 2017.

Voss, K., Holzbeck, P., Pfeilsticker, K., Kleinschek, R., Wetzel, G., Fuentes Andrade, B., Höpfner, M., Ungermann, J., Sinnhuber, B.-M., and Butz, A.: A novel, balloon-borne UV–Vis spectrometer for direct sun measurements of stratospheric bromine, Atmospheric Measurement Techniques, 17, 4507–4528, https://doi.org/10.5194/amt-17-4507-2024, 2024.

800 Wong, K. W., Fu, D., Pongetti, T. J., Newman, S., Kort, E. A., Duren, R., Hsu, Y.-K., Miller, C. E., Yung, Y. L., and Sander, S. P.: Mapping CH$_4$: CO$_2$ ratios in Los Angeles with CLARS-FTS from Mount Wilson, California, Atmospheric Chemistry and Physics, 15, 241–252, https://doi.org/10.5194/acp-15-241-2015, 2015.

Wu, L., Hasekamp, O., Hu, H., Landgraf, J., Butz, A., Aan De Brugh, J., Aben, I., Pollard, D. F., Griffith, D. W. T., Feist, D. G., Koshelev, D., Hase, F., Toon, G. C., Ohyama, H., Morino, I., Notholt, J., Shiomi, K., Iraci, L., Schneider, M., De Mazière, M., Sussmann, R., Kivi, R., Warneke, T., Goo, T.-Y., and Té, Y.: Carbon dioxide retrieval from OCO-2 satellite observations using the RemoTeC algorithm and validation with TCCON measurements, Atmospheric Measurement Techniques, 11, 3111–3130, https://doi.org/10.5194/amt-11-3111-2018, 2018.

Wunch, D., Wennberg, P. O., Toon, G. C., Keppel-Aleks, G., and Yavin, Y. G.: Emissions of greenhouse gases from a North American megacity: Greenhouse Gas Emissions in LA, Geophysical Research Letters, 36, L15 810, https://doi.org/10.1029/2009GL039825, 2009.

Wunch, D., Toon, G. C., Wennberg, P. O., Wofsy, S. C., Stephens, B. B., Fischer, M. L., Uchino, O., Abshire, J. B., Bernath, P., Biraud, S. C., Blavier, J.-F. L., Boone, C., Bowman, K. P., Browell, E. V., Campos, T., Connor, B. J., Daube, B. C., Deutscher, N. M., Diao, M., Elkins, J. W., Gerbig, C., Gottlieb, E., Griffith, D. W. T., Hurst, D. F., Jiménez, R., Keppel-Aleks, G., Kort, E. A., Macatangay, R., Machida, T., Matsueda, H., Moore, F., Morino, I., Park, S., Robinson, J., Roehl, C. M., Sawa, Y., Sherlock, V., Sweeney, C., Tanaka, T., and Zondlo, M. A.: Calibration of the Total Carbon Column Observing Network using aircraft profile data, Atmospheric Measurement Techniques, 3, 1351–1362, https://doi.org/10.5194/amt-3-1351-2010, 2010.

Wunch, D., Toon, G. C., Blavier, J.-F. L., Washenfelder, R. A., Notholt, J., Connor, B. J., Griffith, D. W. T., Sherlock, V., and Wennberg, P. O.: The Total Carbon Column Observing Network, Philosophical Transactions of the Royal Society A: Mathematical, Physical and Engineering Sciences, 369, 2087–2112, https://doi.org/10.1098/rsta.2010.0240, 2011.

Xiao, G., Wang, T., Chen, X., and Zhou, L.: Evaluation of Ship Pollutant Emissions in the Ports of Los Angeles and Long Beach, Journal of Marine Science and Engineering, 10, 1206, https://doi.org/10.3390/jmse10091206, 2022.

Yang, D., Hakkarainen, J., Liu, Y., Ialongo, I., Cai, Z., and Tamminen, J.: Detection of Anthropogenic CO_2 Emission Signatures with TanSat CO_2 and with Copernicus Sentinel-5 Precursor (S5P) NO_2 Measurements: First Results, Advances in Atmospheric Sciences, 40, 1–5, https://doi.org/10.1007/s00376-022-2237-5, 2023.

Zeldovich, J. B.: Okislenie asota pri gorenii i wsrüwach, in: Sobranie trudü: Chimitscheskaja fisika i gidrodinamika, pp. 318–323, Russian Academy of Sciences, 1984.

Zhao, T., Chen, M., and Lee, H.: A Study on the Framework for Estimating Ship Air Pollutant Emissions—Focusing on Ports of South Korea, Atmosphere, 13, 1141, https://doi.org/10.3390/atmos13071141, 2022.

Zhong, Q., Huang, Y., Shen, H., Chen, Y., Chen, H., Huang, T., Zeng, E. Y., and Tao, S.: Global estimates of carbon monoxide emissions from 1960 to 2013, Environmental Science and Pollution Research, 24, 864–873, https://doi.org/10.1007/s11356-016-7896-2, 2017.